Investigation into the production and application of porous titanium within the biomedical field

by

Willem Heber van Zyl

Thesis presented in partial fulfilment of the requirements for the degree of Master of Science in Engineering (Mechanical) in the Faculty of Engineering at Stellenbosch University

Supervisor: Dr Deborah Clare Blaine

December 2014

DECLARATION

By submitting this thesis electronically, I declare that the entirety of the work contained therein is my own, original work, that I am the sole author thereof (save to the extent explicitly otherwise stated), that reproduction and publication thereof by Stellenbosch University will not infringe any third party rights and that I have not previously in its entirety or in part submitted it for obtaining any qualification.

Date: .....

ABSTRACT

In this study, commercially pure titanium foam was produced using space holder powder metallurgy techniques. Titanium foam is attractive as a scaffolding material for bone replacement and implants in the body. The porous morphology of the foam promotes osteogenesis, while the mechanical behaviour of the foam is closer to that of bone, which has an elastic moduli range of 5 - 40 GPa.

Titanium foam was manufactured from powder mixtures of commercially pure titanium (CPTi) powder mixed with 41.4 wt% ammonium bicarbonate (ABC) powder and 1.45 wt% polyethyl glycol (PEG) powder. In this study, two CPTi powders with different particle size distributions, < 75 µm (-200 mesh, designated TiAA) and < 200 µm (-100 mesh, designated TiG), were mixed with the space holder ABC powder, that had been sieved into specified particle size ranges. The size ranges of space holder material studied were: 0 - 710, 250 - 425, 425 - 560, and 560 - 710 µm. This allowed foams with different large or macropore distributions to be produced from the different mixtures.

The mixtures were uniaxially compacted at 100 MPa into transverse rupture bars. The ABC and PEG was then removed by thermal debinding in air for 5 hours at 100 °C and 1 hour at 330 °C each, consecutively. The debound samples are then sintered under high (10^{-6} mbar) vacuum on yttria-stabilised zirconia substrates, heating at 5 °C/min to 1200 °C, with a 2 hour hold at temperature.

The microstructures of the different foams were evaluated by examining the polished samples using light optical microscopy. Three point bend tests were conducted on the sintered bars in order to determine the flexural strength and flexural modulus of the different foams. The produced foams had a relative density range between 37.5 - 62.5 % and average macro pore size range between 300 - 500 µm. The foams were found to have an elastic modulus similar to that of bone, 2 - 7 GPa.

Finally, the mechanical properties of the foams were compared to known open foam mechanical models and other research projects. It was found that: (i) changes in either metal or space holder powder influences the sintering behaviour of metal foams, (ii) sintered titanium foams with similar densities but different macro/micropore size distributions have different mechanical responses to stress and (iii) the Ashby-Gibson model, based on foam density alone, gives a rough estimate of mechanical properties for the titanium foams studied, but does not capture variations due to pore size distribution.

OPSOMMING

In hierdie studie is kommersiële suiwer titaanskuim geproduseer met behulp van ruimtehouer poeier metallurgie tegnieke. Titaanskuim is aantreklik as 'n raamwerkmateriaal vir beenvervanging en -inplantings in die liggaam. Die poreuse morfologie van die skuim bevorder osteogenese, terwyl die meganiese gedrag van die skuim naby aan dié van been is, met ‘n elasticiteitsmodulus tussen 5 - 40 GPa.

Titaanskuim is vervaardig van ‘n poeier mengsel van kommersiële suiwer titaan (CPTi) poeier gemeng met 41,4 gew% ammonium bikarbonaat (ABC) poeier en 1.45 gew% poli-etileenglikol (PEG) poeier. In hierdie studie is twee tipes CPTi poeiers met verskillende deeltjiegrootteverspreiding, < 75 µm (-200 stofdigtheid, TiAA genoem) en <200 µm (-100 stofdigtheid, TiG genoem), met die ruimtehouer ABC-poeier, wat in bepaalde deeltjiegroottereekse gesif is, gemeng. Die wisselende groottes van ruimtehouer wat bestudeer is, was: 0 - 710, 250 - 425, 425 - 560, 560 - 710 µm. Dit het die vervaardiging van skuim met verskillende groot of macroporeuse vanaf die verskillende mengsels toegelaat.

Die mengsel is teen 100 MPa in een rigting gekompakteer. Die ABC en PEG is dan verwyder word deur termiese ontbinding in lug vir 5 uur by 100 °C en 1 uur by 330 °C elk, onderskeidelik. Die ontbinde monsters is dan onder hoë (10^{-6} mbar) leemte op yttrium-gestabiliseer zirconia-substraat, met verwarming teen 5 °C/min tot 1200 °C met 'n verdere 2 uur by 1200 °C, gesinterd.

Die mikrostrukture van die verskillende skuim is geëvalueer deur gepoleerde monsters met behulp van ‘n ligmikroskopie te ondersoek . Driepunt draaitoetse is op die gesinterd stawe uitgevoer om die buigsterkte en buigmodulus van die verskillende skuime te bepaal. Die vervaardigde skuime se relatiewe digtheid het tussen 37,5 - 62,5 % gewissel en die gemiddelde makroporiegrootte tussen 300 - 500 µm gewissel. Die skuim het 'n elastisiteitsmodulus soortgelyk aan dié van been getoon, 2 – 7 GPa.

Ten slotte is die meganiese eienskappe van die skuim met bekende oop skuim meganiese modelle en ander navorsingsprojekte vergelyk. Daar is bevind dat: (i) veranderinge in óf metaal of ruimtehouer poeier beïnvloed die sinteringgedrag van metaalskuime, (ii) gesinterd titaniumskuim met soortgelyke digthede, maar verskillende makro / mikroporeuse verdelings, toon verskillende meganiese reaksies op stres en die Ashby-Gibson model, gebaseer op die skuimdigtheid alleen, (iii) wat 'n rowwe skatting van die meganiese eienskappe vir die bestudeerde titaniumskuime gee, maar nie die variasies ingrootteverspreiding van porieë ondervang nie.

TABLE OF CONTENTS

Page

LIST OF FIGURE

Page

LIST OF TABLES

Page

1. INTRODUCTION

In an ideal world it would be desired that an alternative material for artificial bone implants would have the following characteristics: the material should be biocompatible to ensure the safety of the human body, the material should be able to fulfil the required loading conditions throughout the expected implant period, and, ideally, should encourage bioactivity in such a manner that it aids in the bonding between the implant material and the surrounding bone (Wisutmethangoon, et al., 2008).

Suggestions for the above mentioned ideal alternative materials could be commercially pure titanium (CPTi) and titanium alloys, such as the commonly used Ti-6Al-4V. Titanium is a silvery-white, lustrous metal which is biocompatible, has a relatively low density and is known for its high strength (Wisutmethangoon, et al., 2008). However, due to the mismatch between titanium's and bone's Young's modulus (110 GPa and 10-40 GPa, respectively (Wen, et al., 2001), as well as the mismatch between titanium's and bone's longitudinal compressive strength (434 MPa and 170-193 MPa, respectively (Wisutmethangoon, et al., 2008), it is possible that stress shielding and local reabsorption of bone may occur if the implant is made from pure solid titanium (Imwinkelried, 2007 and Ryan *et al.*, 2006).

Therefore, it is required to alter the mechanical properties of a titanium implant, so that they closely match that of bone. The suggested approach is a continuation of the author's final year project where powder metallurgical techniques were used to produce porous titanium structures (van Zyl, 2010). The author was successful in producing porous titanium structures which had similar characteristics to that of bone, therefore proving the viability of the suggested approach.

Coincidently, when the porous titanium is produced, using the powder metallurgy space holder method, open-cell pores are formed. These pores act like anchoring sites for the native bone to infiltrate and integrate into the porous titanium structure. Additionally, the implant also allows osteoblast growth and vascularisation to occur (Wen, et al., 2001).

This thesis is an in-depth study on the production parameters of a porous titanium structures and how the different parameters influence the final material microstructure and its mechanical properties. During the proposed study, porous structures were produced from CPTi powder mixed with a space holder powder material that decomposes during processing. The material and mechanical properties of these structures were evaluated, and the results were analysed in order to understand the process-property relationships particular to this system

2. MOTIVATION

The need for artificial scaffolding becomes apparent when looking at bone loss due to tumours, infection or trauma. Although these cases are common, the treatment process is not trivial and sometimes not possible if the extent of bone loss becomes great. Using titanium foam as a material for permanent artificial bone scaffolding allows osteoblast growth and vascularisation within the implant (Wen, et al., 2001). If this method can be perfected, it will become possible to produce scaffolds which can be used to replace damaged bone, allowing the patient's bone to regenerate and make a full recovery.

3. OBJECTIVES

The main object of the proposed project is to determine the processing parameters that significantly influence the material properties of porous titanium produced by the powder metallurgy space holder method. In order to do this, a literature study must be conducted to determine which process parameters have currently been identified as parameters that control the material properties of porous titanium. The methods used to determine the sensitivity of these parameters to the material properties must also be researched. Therefore, the following are the initial objectives for the project:

- Isolate specific important process parameters and establish methodologies to determine sensitivity of the parameters on the material properties.
- Conduct experiments according to the established methodologies in order to determine the most sensitive process parameters (sensitivity analysis).
- Use the knowledge obtained from the sensitivity analysis to produce a porous titanium structure with customised microstructure and mechanical properties.
- Establish further research directions for this project that will utilise the results, such as technology transfer for biomedical implant manufacturing.

4. LITERATURE STUDY

A literature study was conducted to establish the current medical procedures for treatment of extensive bone loss, the types of foams that are used for implants, the different production methods of titanium foam, and the current and desired characteristics of titanium foams.

4.1. Bone structure and general mechanical properties

Bone can be considered as an open cell composite material which is largely made up of protein-related materials and complex vascular systems. When taking a cross section of bone it is possible to see that bone has two distinct regions. The outer shell is considered to be comprised of dense compact or cortical bone, while the inner core is comprised of highly porous cellular, cancellous or trabecular bone, as can be seen in Figure 1. The Osteon of the bone are found within the cortical bone and are cylindrical by nature with a diameters ranging between 10 to 500 µm. It should be noted that the Osteon contain blood vessels which run parallel to the bones axis and are connected to the surface through the perforation canals.

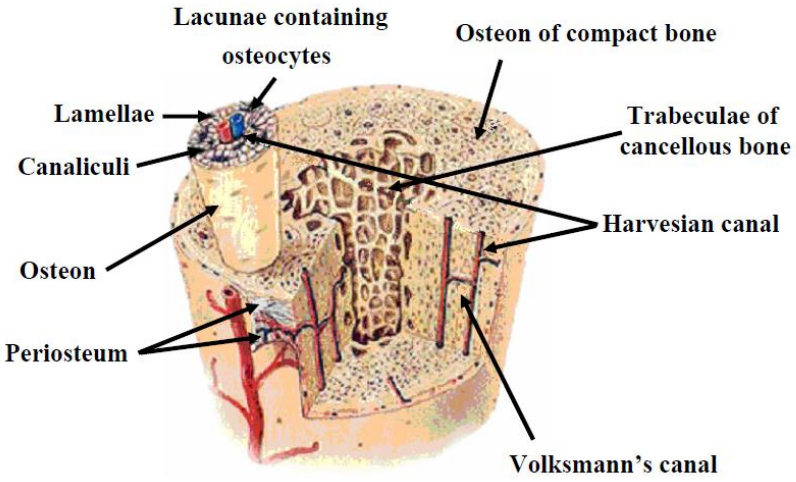

Figure 1: The structure of bone (http://training.seer.cancer.gov/anatomy/skeletal/tissue.html)

The highly porous core of the bone consists of an interconnected network of trabeculae which have diameters ranging between 50 to 300 µm. Due to this structure, the average porosity of cortical bone is 5 to 10 % while that of cancellous bone ranges between 75 to 90 % (Nouri, et al., 2010). This equates to a wet apparent density of 1.99 g/cm^3 (Black & Hastings, 1998) for cortical bone and a substantially varying density of 0.05 to 1.0 g/cm^3 (Black & Hastings, 1998) for cancellous bone. The porosity of cancellous bone is measured by the volume of non-bonelike tissue present within cancellous bone which is usually filled by bone

marrow. The main reason for the large density variation in cancellous bone is because cancellous bone densifies from the center outwards.

Bone contains about 99 % of the human body's calcium reserve. This calcium is stored and converted into bone mineral which is mostly in the form of hydroxyapatite ($Ca_{10}(PO_4)_6(OH)_2$).

To ensure successful scaffolding implantation, it is important that the implant does not only match the biological requirements but also the mechanical properties. Bone can be considered as an anisotropic material with mechanical properties that vary with anatomical location and loading direction. This is illustrated by the large variation in the elastic modulus measured between the longitudinal and transverse directions (Nouri, et al., 2010).

The mechanical strength of cortical bone in the longitudinal direction is reported to be in the range of 79 to 151 MPa in tension and 131 to 224 MPa in compression (Thomson, et al., 1995), with the elastic modulus reported to be in the range of 17 to 20 GPa. However, due to anisotropic nature of bone, the mechanical strength of cortical bone in the transverse direction is reported to be in the range of 51 to 56 MPa in tension and 106 to 133 MPa in compression, with elastic moduli in the range of 6 to 13 GPa (Nouri, et al., 2010). Due to the architectural nature of cancellous bone, the reported mechanical properties vary largely. However, compression strength of 2 to 5 MPa and elastic moduli of 0.76 to 4 GPa are reported (Nouri, et al., 2010).

4.2. Background on medical procedures for extensive bone loss

The current procedure for the treatment of extensive bone loss is bone grafting. Bone grafting techniques are procedures followed in order to replace missing bone, via surgery, with bone of either the patient's own body, an artificial, synthetic or natural substitute. Bone, unlike most tissues, has the ability to regenerate completely if provided with sufficient space. It is common that the native bone should grow into the grafted section, often replacing or integrating to form a region of new bone. In order for a bone grafting material to provide the desired biological function, it should have four fundamental characteristics: osteoconduction, osteoinduction, osteopromotion and osteogenesis (Klokkevold & Jovanovic, 2002).

Osteoconduction is the ability of the bone graft material to serve as a scaffolding material for penetration of the native bone, so that new bone growth can continue and form a new integrated section of bone. This is the primary and most important characteristic of any grafting material (Klokkevold & Jovanovic, 2002).

Oesteoinduction is the ability of the grafting material to promote the osteoprogenitor cells (cells generated within the periosteum and bone marrow) to differentiate into osteoblast cells, which are responsible for bone formation. This characteristic therefore helps to promote faster integration of the bone grafting material and is often achieved by the grafting material having bone

morphogenetics (BMPs) imbedded into the material (Klokkevold & Jovanovic, 2002).

Oesteopromotion is the ability of the grafting material to promote osteoinduction without the presence of osteoinductive properties. This is often achieved through addition of organic elements required for bone growth into the grafting material, such as enamel (Klokkevold & Jovanovic, 2002).

Oesteogenesis is the ability that osteoblasts have to form in the grafting material. These osteoblasts help to contribute to bone growth. For this to occur it should be incorporated with osteoconduction and osteoinduction (Klokkevold & Jovanovic, 2002).

As these characteristics are dependent on the type of bone grafting material used, it becomes important to have predefined categories for all types of bone grafting material. The main categories are as follows: alloplast, xenograft, allograft and autograft (Klokkevold & Jovanovic, 2002).

Alloplast is the category for a synthesised material which is made up of naturally occurring minerals which are essential for the formation and health of bones. These materials include hydroxyapatite, bioactive glass, calcium carbonate, as well as tricalcium phosphate. This category has the characteristics of allowing osteoconduction, with the ability of reabsorption[1] (Klokkevold & Jovanovic, 2002).

Xenograft is the category for a natural grafting material which has its origin from other species, often bovine (cow) material (Klokkevold & Jovanovic, 2002).

Allograft is the category used for bone grafting material received from other human patients. The bones are harvested from the cadavers of patients have donated their bones to bone banks. This form of grafting material can have both osteoconduction and osteoinduction characteristics (Klokkevold & Jovanovic, 2002).

Autograft is the category used for bone grafting material grown or harvested from the patient's body. This is often achieved through a procedure of aiding bone outgrowths, and then harvesting them for implantation or by harvesting non-essential bones. This form of bone grafting material satisfies all bone grafting material characteristics (Klokkevold & Jovanovic, 2002).

It is proposed to use metallic foam as a bone grafting material as it can serve as a bone scaffolding material which allows osteoblast growth as well as vascularisation to occur within the implant (Wen, et al., 2001). Therefore, the metallic foam can be classified as an osteoconduction grafting material. It is a variant of the alloplast, as the foam is created from inorganic materials and implanted within the bone. Unlike xenograft, allograft and autograft, the

[1] Allows the body to absorb all contents of the grafting material

suggested metallic foam can be manufactured to the desired shape and size, and as many times as needed as it is independent of available material resources or donors.

4.3. Metallic foams

As mentioned section 1, the use of titanium for implant material is ideal as it is biocompatible, corrosive resistant and has a high strength-to-weight ratio. The use of solid titanium for implants results in uneven loading of the surrounding bone and as a result can cause stress shielding and local reabsorption of bone (Imwinkelried, 2007 and Ryan *et al.*, 2006). This typically leads to a reduction in the implant lifetime expectancy and, as a result, an alternative solution to using solid titanium implants has been investigated. One suggested alternative to address this uneven loading is to reduce the stiffness of the implant to match that of bone. This is typically done by increasing the porosity, effectively decreasing the mechanical properties of the implant to be closer to those of bone. The production of titanium foam has been widely researched and this will be the focus of this project.

Metallic foams can be characterised into two categories: open-cell and closed-cell foams. The main difference between open-cell and closed-cell foams is that in closed-cell foams each pore is individually covered with a membrane, whereas with open-cell foams the pores are connected, allowing human tissue to grow into the pores and anchor itself (Ryan, et al., 2006). Although both types of titanium foams are usable in biomedical applications, this report focuses on open-cell titanium foams due to their characteristic of allowing bone tissue to infiltrate the pores, giving the scaffolding the desired osteoconduction characteristic.

4.4. Biocompatibility and oxidation characteristics of titanium

Titanium is used for biomedical applications due to it being an attractive material because of its strength, lightness and high resistance to corrosion. Titanium's biocompatibility is based on a thin layer, approximately 5-29 nm, of TiO_2 formed surrounding the surface of the bulk material (Bram, et al., 2006). TiO_2 forms naturally around the surface of the sample as it is exposed to the ambient environment. However, when considering titanium powder, it is important to prevent oxidation or contamination from occurring on the particle surface (via oxidation or other particle contaminates) as this hinders particle bonding during the sintering process. The solution to prevent contamination throughout the sample is to sinter the titanium powder under high vacuum. Following sintering, oxidation of the exposed titanium surface will occur naturally, protecting the titanium from reacting with the body.

An additional problem associated with oxidation is that it is an exothermic reaction. This means that when titanium oxidises, energy is released in the form of heat. When the energy released is sufficient, the surface of the titanium particles may ignite. This ignition may result in an adiabatic flame with temperatures of

approximately to 3400K (Shafirovich, et al., 2008). Therefore, the need for a vacuum furnace is not only to prevent contamination but also to ensure safety.

4.5. Production methods of open-cell titanium foams

There are various methods of producing open-cell titanium foams. The three most prominent methods are: furnace sintered metal powders (Ryan, et al., 2006), solid-state expansion (Spoerke, et al., 2008) and the powder metallurgy (PM) space holder method (Ryan, et al., 2006).

The furnace sintered metal powders method is the simplest fabrication technique. The powder is not compacted before sintering and the only densification which the powder experiences are that which occurs during the sintering of the metal powder. This method is generally used when producing low strength filters and the control of the pore size and distribution is minimal.

The solid-state expansion method involves hot-isostatically pressing powders in the presence of a noble gas. Once pressed the resulting high-pressure gas bubbles are allowed to expand by elevating the surrounding temperature in ambient pressure. The control of the pore size and distribution is slightly higher than that of furnace sintered metals powder method, but still limited to the formation of the gas bubbles and the expansion thereof.

The PM space holder process produces metallic foams by mixing a metal powder with an inorganic space holder powder. The mixture is then compacted into the desired shape, thereafter the space holder is thermally removed through decomposition. The desired external shape is maintained while the desired open-cell pores are created where the space holders used to sit.

The pores created are dependent on, and change with respect to, the morphology of the space holder and metal powder as well as the compaction pressure used. This process is highly versatile: capable of producing metallic foams with up to 80 vol% porosity (Ryan, et al., 2006), allows relative control over the desired morphology of the skeletal structure to optimise for osseointegration (Wen, et al., 2001) and is able to make bone replacement material for almost all types of bones. Therefore, the project will focus on PM space holder methods.

4.6. Selected PM space holder methods

When investigating PM space holder methods, it becomes important to determine what desired characteristics are expected from both the space holder and titanium powder.

The main role of space holder powders is to prevent titanium powder from occupying a certain volume, thus creating porosity in the resultant foam. It is critical that when the space holder is removed, that the volume remains vacated and that the space holder material does not contaminate the titanium. An important aspect relating to contamination is the temperature at which the space holder is removed. As oxidation should be kept to a minimum (to ensure sufficient

particle bonding during sintering) the decomposition temperature of the space holder should be low enough to ensure minimal oxidation to take place within the material. The following are possible space holders which have been used successfully by other researchers: ammonium bicarbonate (NH_4:HCO_3) (Ryan, et al., 2006), urea ($(NH_2)_2CO$) (Wenjuan, et al., 2008), titanium hydride (TiO_2) (Wisutmethangoon, et al., 2008) and a mixture of 93 vol% of naphthalene, 6 vol% of EVA (Poly(ethylene-co-vinyl acetate)) and 1 vol% stearic acid (Chino & Dunand, 2009)..

4.6.1. Size of space holder particle

It is good practise to select a space holder particle size larger than the base material (Nouri, 2008). Typically, the space holder particle size is selected to be in the range of 100-500 μm, which has been shown to produce macropores in the range of 300-400 μm (Arifvianto & Zouh, 2014) and is ideal for osseointegration.

A relationship between interconnectivity and space holder particle size has been determined using tomographic analysis of the macropores (pores formed by the void left behind from decomposed space holder material); it was found that the interconnectivity increases when the space holder particles size increases. This is due to the greater packing coordination number of the larger space holder particles as compared to smaller particles after compaction (Tuncer, et al., 2011).

It was also shown by tomographic analysis that macropore sphericity increases when space holder particle size increases. Lastly, relative porosity increases in scaffolds with larger space holder particle sizes, as the surface area of scaffold decreases when the space holder particle size increases. Typically, this means that the pore wall thickness increases with the increase in space holder particle size for the same relative density foams, resulting in better mechanical properties of the foam (Tuncer, et al., 2011). However, it has conversely been shown that the flexural strength decreases as the space holder particle size increases (Amingo, et al., 2011). All that can be concluded from these studies is that there are multiple variables that are influenced by the space holder particle size, and that these in turn influence the mechanical behaviour of the foam.

4.6.2. Size distribution of space holder particle

It is important for the space holder particle size distribution to be controlled. In most cases, it was found that it is better to have a narrow space holder size distribution. It was found that an unsieved, non-uniform space holder particle size distribution typically results in scaffolds with deteriorated mechanical properties (Arifvianto & Zouh, 2014).

4.6.3. Selected space holder material

Ammonium bicarbonate (NH_4HCO_3), a white powder which is a common space holder used for most PM foam production (Imwinkelried, 2007), decomposes into gas at relatively low temperatures with minimal contamination of titanium powder (Nouri, et al., 2010). It also offers sufficient green strength to the compacted metal powder-space holder powder mixture to make the compacted or green sample rigid enough to be handled without breaking. Ammonium bicarbonate is also easily sieved so that the particle size distribution range remains narrow. This results in a good level of control over the initial parameters of the ammonium bicarbonate powder.

For all of the above reasons, ammonium bicarbonate was selected for the production of the porous titanium in this study

4.7. Selected lubricant material

As most space holders are non-adhesive powders, the addition of a binder and lubricant is deemed necessary to provide sufficient green strength for handling the die compacted powder mixture samples. The lubricant should behave similarly to that of the space holder material, in that it should not contaminate the titanium and but should also be able to decompose at relatively low temperatures (lower than the sintering temperature for titanium). The lubricant is required to prevent delamination (cracking and separation of the compacted powder during the ejection from the die) from occurring due to friction with the die wall.

Polyethylene glycol (PEG) was chosen for this purpose. PEG is supplied in various polymer chain lengths. The selection of PEG 1000 was based on its polymer size and molecular weight. The number following PEG indicates the molecular weight of the PEG in g/mol. As PEG 1000 is a waxy compound with a relatively short polymer chains, it is easily deformed and therefore should flow easily around the powder particles, allowing it to bind and lubricate.

4.8. Sintering theory

Sintering is classified as the bonding of closely packed powder which is heated to temperatures in excess of approximately half of the absolute melting temperature (German, 1985). In addition to particle bonding, sintering can also have the following effects:

- Chemical reactions
- Dimensional changes
- Internal stress relief
- Phase changes
- Alloying

When considering pressure-less sintering, which occurs without the need of an external pressure, the main sintering processes are solid-state and liquid phase processes. Liquid phase sintering is generally required when a powder is difficult

to sinter and liquid needs to be introduced into the sample to aid the sintering process.

Solid-state sintering occurs at the contact points between powder particles by atomic diffusion in the solid state. It relates to a low mass transport rate (the rate at which mass flows between powder particles during sintering). Liquid-phase sintering has a higher mass transport rate due to this higher diffusion rates of atoms in the liquid state. It is additionally aided by the high pressure which is generated due to the capillary pull which is exerted on the particles when the liquid permeates throughout the material (German, 1996).

As this study focuses on the investigation of a single phase powder mixture and titanium is generally easy to sinter, only solid-state sintering will be reviewed.

4.8.1. Solid-state sintering

Figure 2 illustrates the different stages of solid-state sintering.

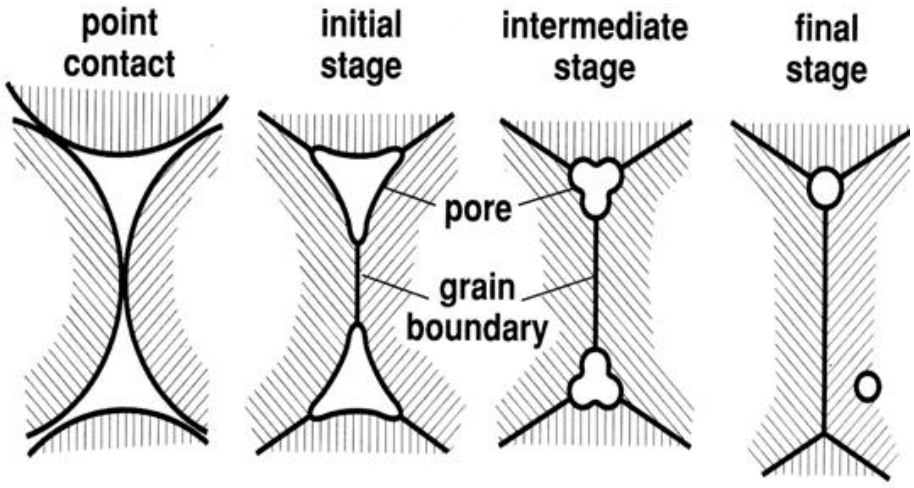

Figure 2: Solid-state sintering stages (German, 1996)

As demonstrated in Figure 2, at the beginning of solid state sintering there are the point contacts between powder particles. During the initial stage, the point contacts begin to fuse as a result of surface diffusion in a process that is typically called “necking”; this necking process results in the pore structure becoming smooth and interconnected. As the process continues into the intermediate stage, grain boundary and volume diffusion dominate and cause significant mass transport between particles. As a result, the pores tend to become cylindrical and elongated, and the average pore size reduces significantly. The final stage of sintering occurs when the pores have pinched off into lenticular or spherical pores and there is less than 8 % porosity remaining (German, 1996).

4.9. Models for the mechanical properties of metal foams

Currently, all proposed models, which are used to characterize the mechanical properties of metal foams, can be categorized into one of three categories:

- Cross-sectional area models,
- Stress concentration models, or
- Effective flaw size models.

For the cross-sectional area model, the critical parameter is that of the actual load bearing area or that of the minimum solid cross sectional area. For the stress concentration model, the shape of the pores is used to estimate the resulting stress concentrations. Lastly, the effective flaw size model is based on the assumption that flaws exist in the vicinity of the pore before final failure (Hattiangadi & Bandyopadhyay, 2000).

4.9.1. Cross-sectional area model

The most commonly used model is that suggested by Gibson and Ashby (a variation on the cross-sectional area model); they model the open cells as a cubic array, as shown in Figure 3, where the cell edges have a square cross-sectional thickness of *t* and a cell length of *L*.

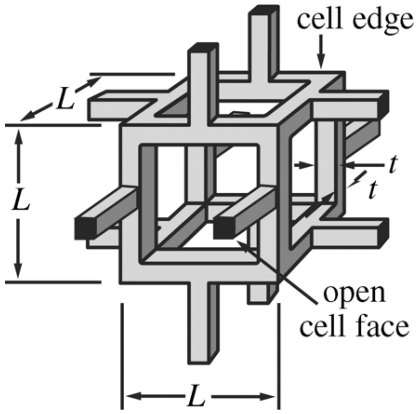

Figure 3: Gibson and Ashby cubic model for open-cell foams (Gibson & Ashby, 1988)

When considering the mechanical properties for this model, it is important to consider a typical stress-strain curve for a cellular solid, shown in Figure 4. The stress relationship has 3 defined stages: the plastic deformation stage, the plateau stress stage and the densification stage.

The elastic deformation stage occurs when the load applied to a cellular solid is sufficiently low to cause recoverable deformation.

The plateau stress stage occurs once the force is sufficient to surpass the elastic deformation stage and plastic or permanent deformation begins. The plateau stress stage is characterised by the cells buckling and crushing as cell edges collapse under pressure. Once the plateau stage is reached, a relatively minimal increase in stress will result in a relatively large increase in strain. This buckling and crushing of the cells gives the curves the typical plateau characteristics and results in permanent deformation with relatively large energy absorption.

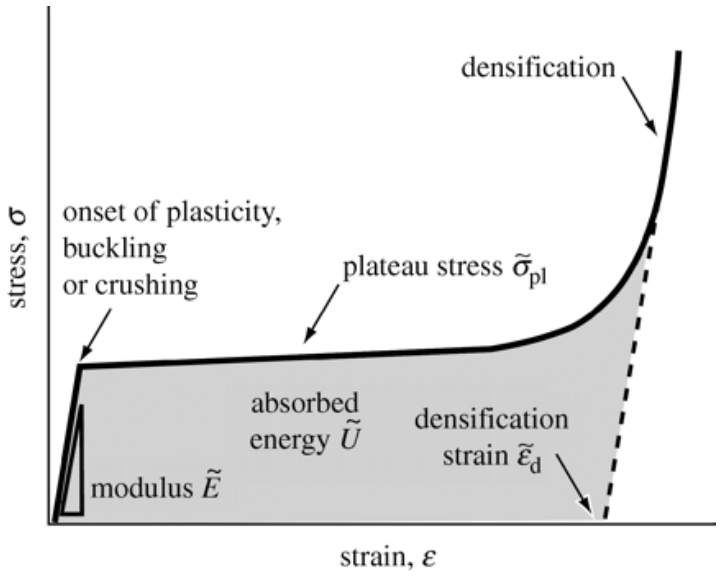

Figure 4: A typical stress-strain curve for a cellular solid or foam (Gibson & Ashby, 1988)

Once the buckling and crushing of the cells reaches a point where the force required to cause further deformation increases dramatically, the material enters the densification stage. This stage typically occurs as a result of large portions of the void volume within pores being collapsed and therefore the material rearranges itself and densifies.

The cubic array in Figure 3 is an idealisation of a unit cell structure, which consists of solid struts which have a low thickness to length ratio ($t << L$). Considering this cell structure, cellular solids can be characterized by their relative density, which is related to the cell dimensions as follows:

$$\frac{\rho}{\rho_s} \propto \left(\frac{t}{L}\right)^2 \tag{1}$$

Where:

ρ = density of open-cell foam ($\frac{Kg}{m^3}$),

ρ_s = density of material solid ($\frac{Kg}{m^3}$),

t = thickness of cell edge (m),

L = cell size (m).

This model is based on the theoretical micro-mechanical assumptions made, while the parameter values are identified by mean of experimental data. This mean the Ashby-Gibson captures any morphology or alternate influence via the parameters values which are identified from experimental data.

4.9.2. Elastic deformation

Figure 6 shows the deformed cubic cell that results from loading the original cubic array, shown in Figure 3, with an applied load, *F*. The loaded force, *F*, is as

a result of the remote compressive stress, σ, within the specimen as a whole. This force, which is applied to the cell edges, will cause the cell edges to bend, which results in a perceived low modulus of elasticity for cellular solids. The deflection of the cell strut due to bending is described by, δ, as indicated in Figure 5.

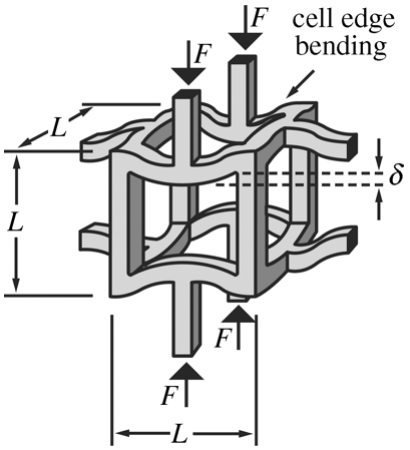

Figure 5: Graphical representation of a loaded Ashby-Gibson open-cell foams model (Gibson & Ashby, 1988)

Under these loading conditions, beam deflection theory is applied as the loading case is similar to that of a simply-supported beam with a mid-point load along its length of L. Thus, the mid-point deflection is given by:

$$\delta \propto \frac{FL^3}{E_s I} \tag{2}$$

Where:
F = applied force (N),
L = length of cell (m),
E_s= elastic modulus of solid material (Pa),
I = the second moment of area (m^4),
δ = the deflection of the cell edge(m).

As the forces being applied are a result of the compressive stress within the material, the force is described by $F \propto \sigma L^2$. The second moment of the area of the cell edge is based on the cross-sectional area of the cell edge and is therefore described as $I = t^4/12$. The compressive strain experienced in the foam as a whole is $\varepsilon \propto 2\,\delta/L$.

The elastic modulus of the open-cell foam, E, relates the stress to the strain,

$$E = \frac{\sigma}{\varepsilon} \tag{3}$$

Combining these relationships with equations (1) and (2), shows that the elastic modulus of the open-cell foam is related to the elastic modulus of the solid material by the square of the relative density,

$$\frac{E}{E_S} = C_1 \left(\frac{\rho}{\rho_s}\right)^2 \tag{4}$$

Where:
E = elastic modulus of open-cell foam (Pa),
E_S = elastic modulus of the solid material (Pa),
ρ = density of open-cell foam ($\frac{Kg}{m^3}$),
ρ_s = density of material solid ($\frac{Kg}{m^3}$),

The constant, C, is dependent on the geometry of the mechanical model used, but it generally assumed to be relatively close to unity.

4.9.3. Failure mechanisms

When modelling a cellular structure which is subjected to a collapse force, a force which drives the material beyond the elastic deformation stage, there are three main forms of failure which result in permanent deformation (Gibson & Ashby, 1988):

- bending,
- buckling, and
- fracture.

All three of these forms of failure result in the cell edges collapsing and in turn gives the typical open-cell stress strain curve its characteristically plateau stress shape.

Typically, it is expected that bending-dominant behaviour will occur in foams made from ductile materials. Buckling-dominant behaviour will occur in elastomeric foams and fracture-dominant behaviours will occur in brittle foams. As this study focuses on titanium, which is a ductile material, only the bending-dominate behaviour failure will be determined. Elastomeric foams are typically made from polymers and brittle foams from ceramics (Gibson & Ashby, 1997).

4.9.4. Permanent deformation: bending-dominant yielding

Under bending-dominant failure, it is assumed that the collapse force applied to the cellular structure creates a plastic hinge at the cell corners. At the hinge points, a fully plastic moment occurs and, as a result, permanent deformation occurs. Figure 6 highlights these plastic moment hinges and shows where they typically occur.

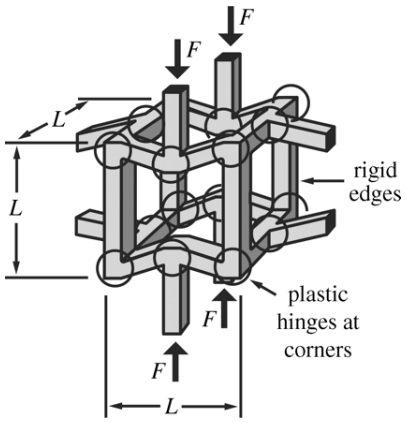

Figure 6: Graphical representation of a loaded Ashby-Gibson open-cell foams model and the points where the momentum causes plastic deformation (Gibson & Ashby, 1988)

The expected plastic moment which occurs due to the remote stress applied to the sample is related to the yield strength of the solid material as follows,

$$M_f \propto \frac{\sigma_{y,s} t^3}{4} \tag{5}$$

Where:
M_f = plastic moment (Nm),
$\sigma_{y,s}$ = yield strength of solid material (Pa),
t = thickness of cell edge (m).

When considering that the moment is related to the remote stress by $M \propto FL \propto \sigma L^2$ (Gibson & Ashby, 1997), it is possible to combine these relationships and to relate the plateau stress to the yield stress of the solid materials through the relative density:

$$\frac{\sigma_{pl}}{\sigma_{y,s}} = C_3 \left(\frac{\rho}{\rho_s}\right)^{\frac{3}{2}} \tag{6}$$

Where:
σ_{pl} = plateau stress (Pa),
$\sigma_{y,s}$ = yield strength of solid material (Pa),
ρ = density of open-cell foam ($\frac{Kg}{m^3}$),
ρ_s = density of material solid ($\frac{Kg}{m^3}$).

Typically, the constant in equation (6) is approximately 0.3 for metal foams (Gibson & Ashby, 1988).

4.10. Published studies for titanium foams

Table 1 is a summary of work conducted by other researchers. Although this is not an exhaustive summary, it gives a good indication of the general trends and production parameters used. All of these studies focused on the production of titanium foams using commercially pure titanium powder as the scaffold material and ammonium bicarbonate as a space holder material.

Table 1: A summary of published studies for titanium foams

	Sources		
Characteristics	(Thomson, et al., 1995)	(Wen, et al., 2001)	(Amingo, et al., 2011)
Titanium powder	Commercially pure titanium grade 4	Commercially pure titanium grade 4	Commercially pure titanium grade 3
Titanium powder particle size (µm)	<45	<45	<45
Compaction Pressure (MPa)	Not specified	100	100, 200
Decomposition Temperature (ºC)	95	200	80
Decomposition duration (hours)	12	5	21
Sintering Temperature (ºC)	1300	1200	1300
Sintering duration (hours)	3	2	2
Space holder particle range (µm)	425-710	200-600	250-500, 500-1000
Yield Strength (MPa)	60-70	35	90-500
Elastic modulus (GPa)	7-14	5.3	21-100
Macropore size (µm)	100-500	200-500	Not specified
Porosity range (%)	50-80	78	25-62.5

From this brief comparison, as well other studies not reported here, it seems that the production parameters of titanium foams are not standardized. The diversity of production parameters in published literature has also been noted in a review on porous titanium (Arifvianto & Zouh, 2014).

5. METHODOLOGY AND EXPERIMENTAL OVERVIEW

In this section an overview of the typical production cycle and the experimental methodology is given. An explanation of the procedures for each typical experiments conducted at each process step follows.

5.1. Production cycle

5.1.1. Production selection

For this study, titanium foams are produced using the PM space-holder process. The typical process is shown in Figure 7, with each process step labelled. A short description of each process step is given in subsequent sections. These steps are independent of the metal powder and space holder powders used. However, for this study, titanium powder was used with ammonium bicarbonate powder as the space holder material.

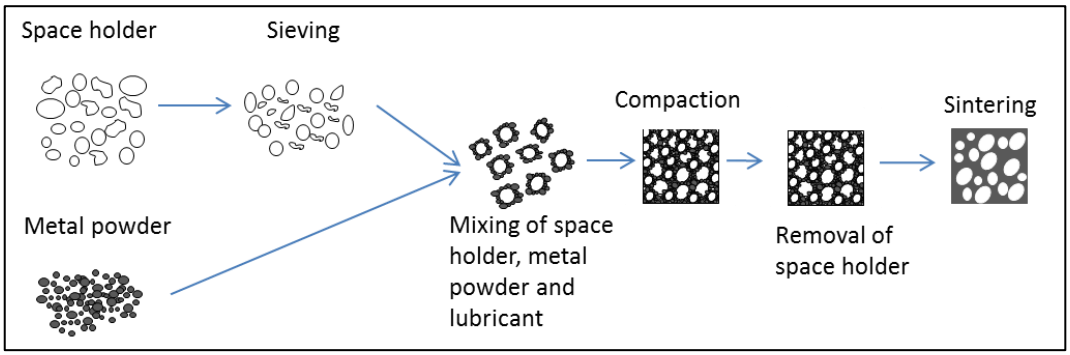

Figure 7: Production steps for porous titanium using the PM space holder method.

5.1.2. Sieving

The goal of this study is to determine the effect of the space holder particle size on the structure and properties of the titanium foam. It is also crucial, as mentioned in section 4.6.2, that the space holder particle size distribution be as narrow as possible. For both these reasons, the space holder material, ammonium bicarbonate powder, was sieved into batches of specific particle size ranges. This allows the macropore size, post sintering, to be controlled so that foams with specific pore size distributions can be manufactured. Macropores are the larger pores that initiate from the voids left by the decomposed space holder material after debinding and sintering. Micropores are the natural inclusion formed due to void formed between the packing of titanium powder, which is common in powder metallurgy especially in low compaction pressures it is more common.

During sintering, as the metal powder particles bond together, the gaps between the powder particles shrink and leave micropores in the sintered material. The relationship between space holder particle size and the size of the macropores is also influenced by the micropores present in the sintered material. Micropores

sometimes connect the voids left by the previous space holder material, resulting in macropores that are larger than the specified space holder particle sizes. These factors are considered when determining the relationship between the space holder particle size range and the macroporosity of the foam.

Sieving is a mechanical method of sorting powders by vibrating the powder through various sized sieves. The standard method for sieving the powder into batches with known particle size ranges (ASTM Standard C136, 2006). It is the method that was used to produce the space holder material batches for this study.

From literature it is suggested that the desired space holder particle size, based on similarity to the structure of bone, is in the range of 425-710 µm (Imwinkelried, 2007). It is important that a large spectrum of particle size batches is sieved to allow investigation of the effect that the space holder particle size has on the final mechanical strength.

5.1.3. Mixing

For mixing, it is important that an even distribution between the different constituents (metal powder, space holder and lubricant) is obtained. The metal powder determines the resultant sintered network of the foam. The space holder powder is responsible for the creation of the macropores and the lubricant helps to reduce die wall friction during compaction. If the mixture is not homogeneous (evenly distributed), the space holder powder could coagulate and cause uneven pore distribution and possibly the creation of larger pores, introducing weak points into the foam.

A mixing study is conducted to determine the mixing time at various mixing speeds required to produce a homogeneous powder mixture. The homogeneity is evaluated by measuring the apparent density, at various stages during mixing. Apparent density is the density of the loose powder mixture, as it fills a specified volume. It is measured without tapping or settling the powder, under the force of gravity alone.

Due to the large difference in densities of each powder constituent, any non-homogeneity in the powder mixture will result in a significant difference in its apparent density. Therefore, once the apparent density of the mixture stabilises, it is considered to be homogeneous.

5.1.4. Compaction

Uniaxial die compaction is used to form the powder mixture into a desired green shape. Typically, a tooling set consists of an upper punch, lower punch and die. The compaction step can be broken into 3 stages: filling, pressing and ejection, as shown in Figure 8 (van Zyl, 2010).

A compressibility study is conducted to determine the relationship between compaction pressure and green (compacted) density. This information can then be used to determine the mass of powder mixture required to produce a sample with a specific volume (length, width and height) at a given compaction pressure.

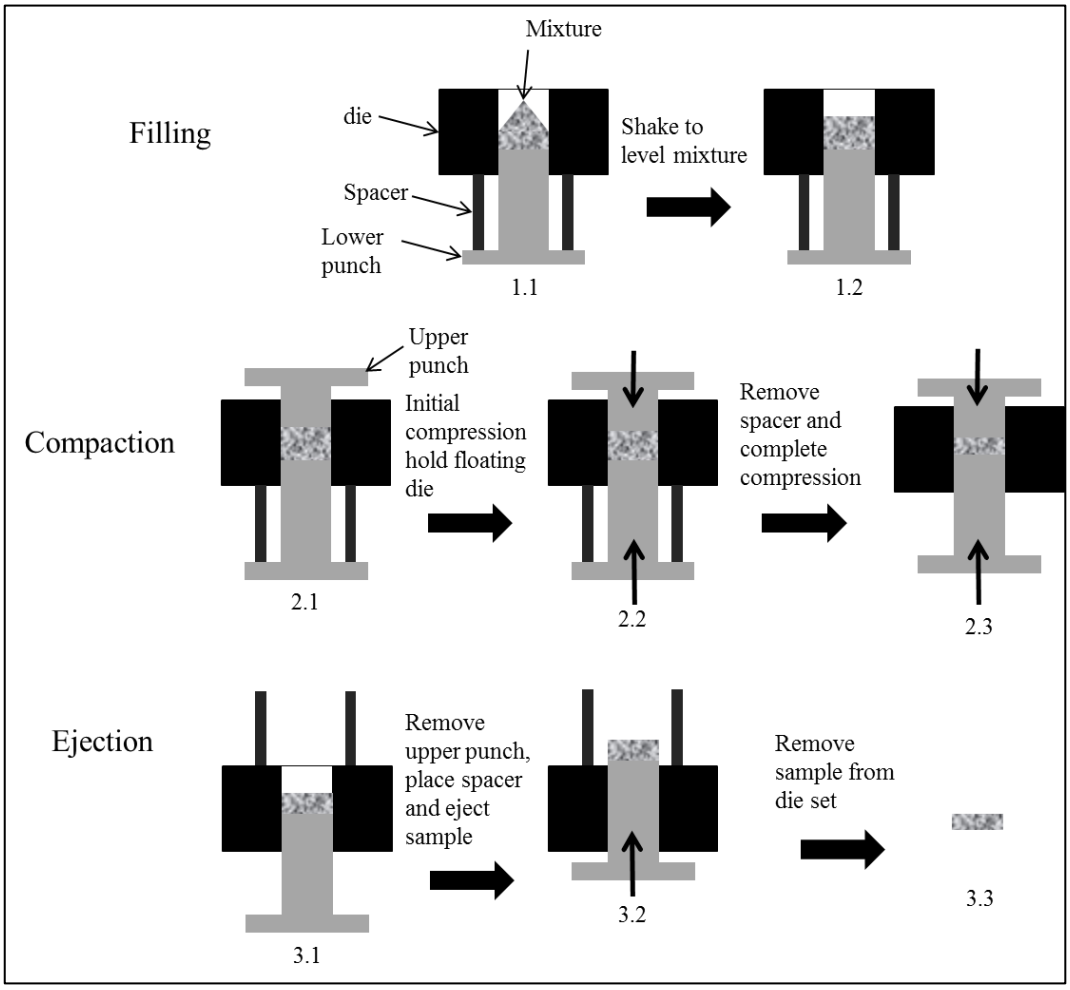

Figure 8: Illustration of compaction procedure

During the filling stage, the lower press is lowered, the die cavity is filled with powder, and the die is shaken and tapped until the powder is relatively level (Figure 8, 1.1 and 1.2). This is done to ensure that during the compaction stage the powder flows evenly throughout the sample and no density gradients occur. As density gradients will result in non-uniform shrinkage during the sintering process.

During the compaction phase the upper and lower punches are moved together inside the die, thus pressing the powder into the desired shape. The density of the compact increases significantly during this step.

During the ejection phase the die is moved down, thus ejecting the green compact from the die. After ejection, all burrs are removed from the green compact's edge using fine sand paper.

5.1.5. Space holder removal

Both the space holder and the lubricant must be removed from the compact before sintering. This is achieved through thermal decomposition. It is important that both the lubricant and the space holder are chosen so that thermal decomposition occurs at temperatures below the critical oxidation temperature of the metal powder. These temperatures are often relatively low compared to the required temperatures for sintering.

As the space holder material makes up a large volumetric fraction of the samples, it must be removed slowly, so as to prevent the surrounding compacted titanium powder from distorting, cracking or blistering. TGA (thermogravimetric analysis) is conducted on both the space holders and the lubricant to determine the optimal temperature of decomposition. The actual decomposition temperature set on the furnace is chosen approximately 10 % below the optimal decomposition temperature so as to ensure that there is no pressure build-up due to degassing of the space holder material during decomposition. Pressure build-up can cause cracking and blistering of the sample.

To ensure that all space holder and lubricant were successfully removes, the mass of the sample were compared before and post debinding. Once the space holder is removed the weight of the sample should match that of the expect weight of titanium added to each sample.

Additionally TGA is conducted on the titanium powder to determine the critical oxidation temperature. The critical oxidation temperature is the temperature at which the rate of oxidation starts increase significantly.

5.1.6. Sintering

After space holder removal, the titanium parts are sintered in a vacuum furnace. During sintering, the titanium particles bond with each other and densification of the skeleton structure occurs. During this densification phase, the macropores shrink in average diameter while still remaining large enough to fulfil the requirements as stipulated in section 5.1.2.

Titanium must be sintered in a vacuum furnace because it is very reactive with air (nitrogen and oxygen) above 500 ºC. Therefore it is critical that special care is taken during the sintering process. Typically, a vacuum less than 10^{-6} mbar is needed to ensure clean sintering of titanium. During the sintering process, the samples are placed inside yttria-stablised zirconia crucibles and inserted into the furnace. Yttria-stablised zirconia is a very stable oxide and so does not react with the titanium during sintering.

5.2. Experimental overview

Figure 9 describes both the production steps as well as the experiments which were conducted to evaluate the material properties at each step. It takes the form of a production flow chart and is used to guide the experiments for this research.

Dashed lines indicate the path following an incorrect outcome or failure, where the solid lines the path following a successful outcome or progress. The highlighted blocks are the production processes and the clear blocks indicate evaluation experiments. The proceeding sections will follow this flow diagram sequentially according to the production procedure (highlighted blocks).

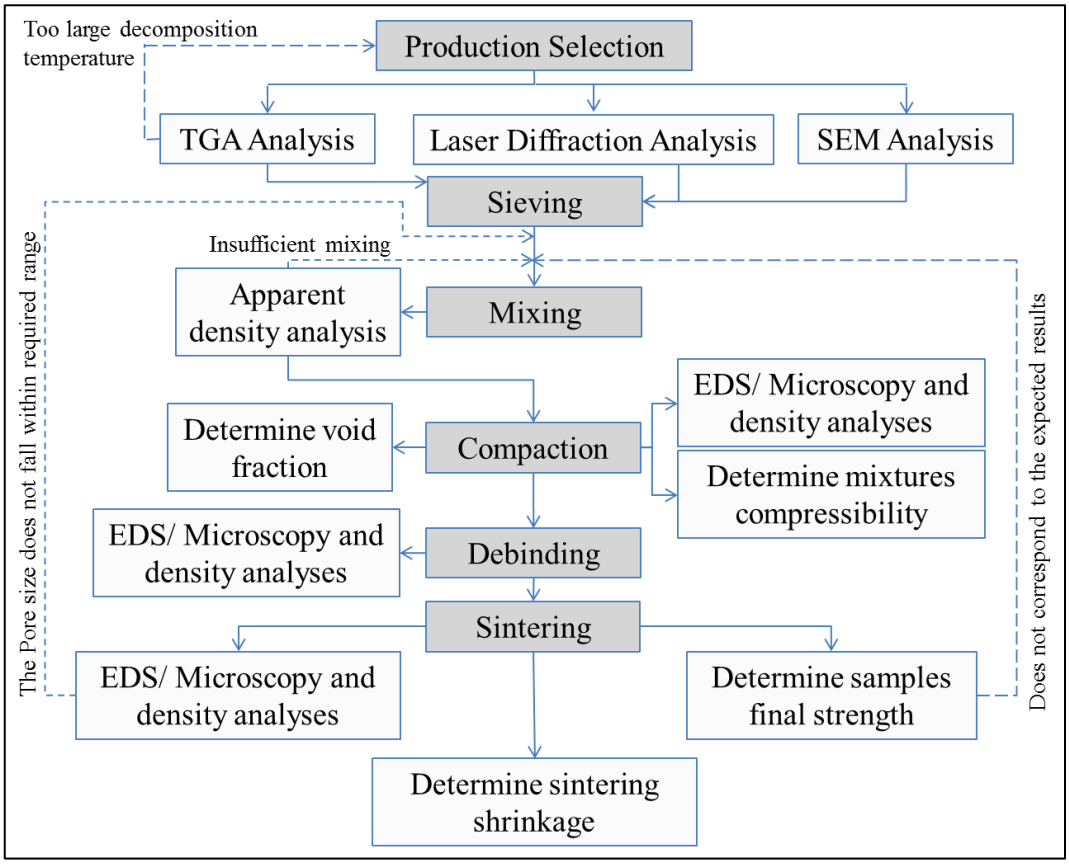

Figure 9: Flow diagram of project overview

5.2.1. Production selection

Two commercially pure titanium powders with different particle size distributions were selected for this study. The as-supplied powder analysis data is shown in Table 2. Both titanium powders were created using the HDH process (hydride-dehydride), a process where the titanium powder is made brittle via hydrogen and then is crushed.

Table 2: Titanium powder characteristics as supplied by supplier

Characteristics	TiAA	TiG
Purity	≥ 99.4 %	≥ 99 %
Particle size	≤ 75 µm	≤ 150 µm
Production method	HDH	HDH
Morphology	Angular	Angular

As mentioned in the section 4.6, the space holder material selected is ammonium bicarbonate (British pharmacopoeia BP E503, purity ≥ 98 %). As ammonium bicarbonate is a non-adhesive powder, the addition of a binder and lubricant was necessary. Both the ammonium bicarbonate and binder/lubricant were chosen to decompose at relatively low temperatures and to not contaminate the samples as they are removed. The binder/ lubricant was PEG 100 for reasons explained in section 4.7.

SEM (Scanning Electron Microscope) imaging

The morphology of the powders were observed using SEM imaging. Knowledge of morphology is important as it determines and affects the processing parameters and material properties of the final product.

SEM uses a high energy electron bean to scan a sample's surface in a raster pattern. Unlike a conventional light microscope, SEM is capable of producing images on multiple planes. In essence, SEM is capable of generating images which giving the illusion of depth and curvature. This is ideal when studying loose powders as well as the pore structure of the foams as they are better visualised in three dimensions.

The SEM analysis was conducted at Stellenbosch University's Central Analytical Facility (CAF) at the Department of Geology, using a ZEISS EVO MA15VP SEM. Both the ammonium bicarbonate and titanium powder was imaged and analysed at various magnifications and areas. SEM analysis was not conducted on the PEG, as PEG is a waxy compound with minimal structural integrity. During the compaction process, all PEG will deform and flow between the other powder particles acting as a lubricant and having minimal effect of the porous structure of the sample.

Particle size analysis by Laser Diffraction

Laser diffraction was used to determine the particle sizes of the different titanium powder used for this research. The particle size distribution of the titanium powder is important as it determines and affects the process parameters and characteristics of the final product.

Laser diffraction analysis is conducted by passing powder particles though a laser beam and measuring the diffraction patterns cause by each particle. The analysis is based on the theory of Fraunhofer diffraction, which states that the particle size is directly proportional to the intensity and angle of the light which is scattered by the particle.

The laser diffraction analysis was conducted at the Department of Chemical Engineering at Stellenbosch University,using a Micromeritics Saturn Digisizer 5200 V1.0 S/N 216.

Thermogravimetic analysis (TGA)

Due to the selection of polyethylene glycol (PEG) as a compaction lubricant and ammonium bicarbonate as space holder, it becomes crucial to know the polymers' thermal degradation characteristics compared to the titanium powders oxidation characteristics. To determine the different materials' thermal characteristics, thermogravimetric analysis (TGA) was conducted for both PEG and the ammonium bicarbonate. It is fundamentally important that both decomposition temperatures of the ammonium bicarbonate and the PEG 1000 are lower than the onset oxidation temperature of the titanium powder. If the decomposition temperatures are not lower, it would mean that the titanium powder would oxidise during the space holder and binder/lubricant removal stage. Although this problem can be overcome by removing the binder in vacuum, this requires the vacuum furnace and pumps to be specially designed in order to prevent contamination and fouling of the furnace and pumps due to outgassing of the polymers as they decompose.

During TGA analysis, a material sample receives energy via the addition of heat (increase of temperature), and the mass and temperature of this sample is monitored during the process. In the case of a polymeric material, sufficient thermogravimetric analysis energy is supplied to break its internal bonds (depolymerisation). Once the bonds are broken and depolymerisation occurs, the polymer experiences a phase change from a solid to a gaseous form which results in mass loss. The mass and temperature of the material under analysis is monitored relative to that of a calibration sample (usually a sapphire crystal). Through manipulation of this data, it becomes possible to acquire a graphical representation of a polymer's behaviour with respect to temperature (thermal degradation characteristics). Similarly, the oxidation characteristics of the titanium powder can be plotted due to the increase in mass of the titanium powder during the onset of oxidation.

The TGA analysis for polymers was conducted through Stellenbosch University's Central Analytical Facility (CAF) at the Department of Inorganic Chemistry. The analysis of both ammonium bicarbonate and PEG were conducted on a TA Instruments Q500 thermogravimetic analyser. Each specimen was analysed twice, once in normal atmosphere (air) and the other in an inert atmosphere (argon), heating from room temperature to 500 ºC. The TGA analysis of the titanium powder was conducted by the Department of Chemical Engineering at Stellenbosch University, using a Mettler Toledo TGA 1 thermogravimetic analyser. The titanium was tested in both air and oxygen atmospheres, heating from room temperature to 500 ºC.

From the results of the TGA analysis it was possible to determine the optimal degradation temperature by taking the derivative of the percentage mass loss with respect to temperature. The temperature at which the derivative peaks is taken as the optimal degradation temperature. Using this information the required temperatures and durations needed to remove all space holder and lubrication materials were determined.

Energy Dispersive Spectroscopy analysis

Along with imaging, the ZEISS SEM is capable of conducting an Energy Dispersive Spectroscopy (EDS) analysis. EDS is an analytical technique used for elemental analysis. EDS determines the different elements present via the interaction between electromagnetic radiation and matter. This is based on the fundamental principle that all mater has a unique atomic structure and therefore reacts differently in the presence of electromagnetic radiation.

EDS analysis was conducted on all titanium powders as to verify the chemical composition of the powders and ensure it matched the specifications of the suppliers. It also gives us a point of reference with respect to the amount of contaminants which are introduced during the production process.

5.2.2. Sieving

The space holder powder, ammonium bicarbonate, was sieved into batches using six sieves (Endecott ∅200 mm woven wire mesh test sieves, mesh sizes of 108, 180, 150, 250, 425, 560 µm) stacked in a shaker (Endecott Minor M200) . The mass of the powder was weighed with a high precision scale (model: FX-120i manufactured by A&D Company LTD) with a resolution of 0.01g.

The sieves were stacked from the largest mesh size (710 µm) to the smallest mesh size (108 µm). All ammonium bicarbonate powder was placed into the top, largest mesh sieve and the sieve stack was secured to the shaker. The shaker aided in allowing the ammonium bicarbonate powder passing through the sieves by mechanically vibrating the sieves, this in turn also helped break up coagulated powder which improved the sieving process.

Table 3: Space holder particle size distributions

	Particle size distributions (µm)						
Space holder (max. particle size)	< 108	108 - 150	150 - 180	180 - 250	250 - 425	425 - 560	560 - 710

Each individual space holder particle size batch was stored in individual airtight container until used for mixing.

5.2.3. Mixing

As explained in section 5.1.3, the mixing process consists three phases:

i. calculating and weighing out the quantities of each mixture constituent,
ii. mixing the constituents together thoroughly, and
iii. evaluating the mixture homogeneity by measuring apparent density.

Details of each phase follow.

Determining mixture constituent ratios

As it is desired to design titanium foams with characterises similar to that of bone, it is fundamentally important to determine what parameters are most critical. A well-known model for predicting strength of foams was generated by Gibson & Ashby (1997). The model relates the strength of foams to their relative density, the ratio of the foam's density to that of the solid material's density. However, as the Ashby and Gibson model was designed for foams with low porosities (high relative density), its accuracy decreases as the porosity increases (or as the relative density decreases). The mechanical behaviour of bone in reaction to an applied compressive stress results in compression of the bone as the applied load increases up to a threshold or plateau strength level. Once the plateau strength is reached, the foam starts to collapse in on itself. As a result, there is a period during which the strain increases without an associated increase in applied force. This period correlates to the threshold or plateau strength of the foam. This phenomenon occurs in natural bone; Wen *et al.* (2001) was able to produce titanium foams that exhibited similar mechanical behaviour. These foams had reported plateau strengths of 35 MPa (Wen, et al., 2001). This plateau strength in combination with the Ashby and Gibson model was used to estimate the required foam density needed to produce specimen similar to that of bone.

The Gibson and Ashby model for plateau strength is:

$$\frac{\sigma_{pl}}{\sigma_{ys}} = C\left(\frac{\rho}{\rho_s}\right)^{\frac{3}{2}} \tag{7}$$

where

σ_{pl} = desired plateau strength, MPa,
σ_{ys} = yielding stress of solid metal, MPa,
ρ_s = density of solid metal, g/cm^3,
ρ = density of metal foam, g/cm^3,and
C = model constant.

Rearranging equation (7) to solve for the required foam density, and using a value for pure solid titanium of 692 MPa for the yield stress, C = 0.3 and 4.51 g/cm^3 (Wen, et al., 2001) for the density, indicates that to obtain a plateau strength of 35 MPa, the titanium foam must have a density of 1.376 g/cm^3 . This is used as the design parameter for the final sintered density of the titanium foam, and correlates to a relative density of 30.3 %.

All mixtures studied were therefore designed to correlate to a final relative density of 1.376 g/cm^3 (30.3 % relative density), with only the particle size distribution of the ABC space holder being varied. In other words, the mass fraction of each constituent is the same for each mixture.

In order to estimate the mass fractions of each constituent, the void fraction of the specimen and also the expected shrinkage during sintering must be determined. Based on previous research, a titanium foam with 30 % void fraction (60 %

relative density) experiences 10 % isotropic shrinkage over thermal debinding and sintering (van Zyl, 2010).

The procedure for obtaining the mass fraction of each constituent is explained in Appendix A. The mass for each constituent is scaled, according to the mixture constituent ratio, in order to produce a specific batch size (mass). The batch size is chosen to be sufficient in order to produce all samples needed for the analysis.

Mixing of constituents

Prior to mixing, each constituent of the mixture (metal powder, space holder and lubricant) was weighed out using a precision scale (model: FX-120i manufactured by A&D Company LTD) with a resolution of 0.01 g. The different constituents are then placed into a closed cylindrical container (typically occupying less than 25 vol% of the container) and mixed at 60 rpm for 8 - 12 min using a 3D turbula-like powder mixer, Figure 10, which was designed (Marais, 2007) and optimised (Ellis, 2008) by two final year students of Stellenbosch University.

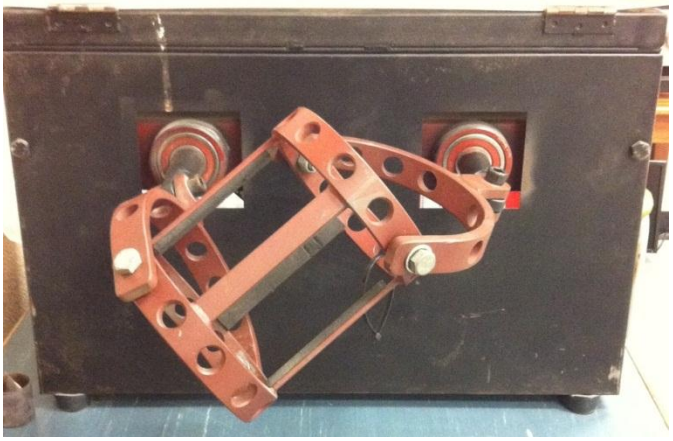

Figure 10: Mixing apparatus which will be to mix the different constituents.

Apparent density analysis

The apparent density of the mixture is measured according to standard (ASTM Standard B417, 2000) using a precision scale (model: FX-120i manufactured by A&D Company LTD) with a resolution of 0.01 g. Three powder mixture samples were collected and analysed after every 2 min of mixing. Emphasis is placed on ensuring that all three samples are taken from different areas within the container, i.e. first sample is taken off the top layer, second from the middle section and final measurement from the powder lying on the bottom of the container. The powder mixture is deemed to be homogeneous if the apparent density does not vary with more than 1 % between samples.

5.2.4. Compaction

The powder mixture was compacted into rectangular transverse rupture bars (TRB) using a CARVER manual 12 ton hydraulic press. The tooling set was

designed according to the ASTM standards (ASTM Standard 925, 2003) (ASTM Standard B528, 2005).

All specimens were compacted at a constant 100 MPa. This pressure correlates to the pressure applied to the projected area of the TRB and was controlled by the relative hydraulic ram pressure. The ram pressure is read from an analogue pressure gauge, and correlated to the related compaction pressure applied to the powder compact from a conversion table. Through visual inspection of the gauge, the related compaction pressure could be controlled to an accuracy of ± 5 MPa.

Each TRB specimen was compacted using 5 g of mixture, weighed out on a FX-120i manufactured by A&D Company LTD with a resolution of 0.01 g. After compaction, the mass and dimensions of the samples were recorded. The green density of the TRBs was calculated as the mass divided by the calculated compacted volume. This process was repeated for each powder mixture of different space holder particle size range.

Dimensional analysis

The aim of a dimensional analysis is to determine the shrinkage of the samples during thermal debinding and sintering, relative to the green state. The dimensions are measured using a digital Vernier micrometer (range 0-150 mm, resolution 0.01 mm) at each stage, from green to brown to sintered state. The shrinkage is calculated similarly to engineering strain as:

$$Shrinkage\ \% = \frac{Original\ length - new\ length}{Original\ length} \times 100\ \% \tag{8}$$

Density analysis

The density of the green, brown (defined in section 5.2.5) and sintered samples were determined by the Archimedes principle according to ASTM standards (ASTM Standards B328, 2003) measures on a precision scale (model: FX-120i manufactured by A&D Company LTD) with a resolution of 0.01 g.

The relative density of the sample is calculated as the ratio of the foam density to the density of 100% dense titanium, 4.51 g/cm^3 (Wen, et al., 2001). The porosity was calculated from the relative density, $\frac{\rho}{\rho_s}$, as

$$porosity\ \% = \left(1 - \frac{\rho}{\rho_s}\right) \times 100\ \% \tag{9}$$

where

ρ = density of specimen, g/cm^3,

ρ_s = density if solid titanium, g/cm^3.

Note that the porosity is only a valid parameter in the brown and sintered samples. In the green samples, the density of the specimen includes the density of the space holder and lubricant materials, as well as that of the titanium powder. In the green state, the calculation of porosity would not give an accurate representation of the actual porosity, or void fraction of the material.

Determining void fraction

In all die compacted powder metallurgy parts, small voids exist between the metallic powder particles. The voids are dependent on the powder morphology, particle packing and compaction pressure. These voids make the sample less dense, increasing the compacted samples volume. This effect needs to be taken into account during the design phase and be defined as a variable, void fraction. The void fraction is required to convert volume percentage base mixing ratio to mass percentage based mixing ratio for the powder mixture.

To determine the void fraction, the theoretical volume is compared with that of the actual volume obtained of the samples. The theoretical volume is the volume which a compacted sample would have if it was assumed to be fully dense (100 % dense with 0 % void fraction). The theoretical volume is thus a function of the theoretical density, which is calculated from the mass fractions of each component in the powder mixture.

$$Theorectial\ volume = \frac{Mass\ of\ sample}{Theorectial\ densinty} \tag{10}$$

The actual volume was determined by Archimedes principles and the differences in the volumes between the theoretical and the actual volumes would be used to determine the void fraction:

$$Void\ fraction = \frac{Actual\ volume - Theorectial\ volume}{Actual\ volume} \tag{11}$$

SEM analysis

The TRB samples were observed using SEM, as explained in section 5.2.1, in order to determine the pore shape and distribution within the compacted sample. As the SEM image generated gives the illusion of depth, the shapes of the pores as well as their diameters are easily observed.

5.2.5. Debinding

During the debinding process, the space holder and binder, ammonium bicarbonate and PEG, respectively, are thermally decomposed and thus removed from the green sample. The green samples were debound by heating them in a retort furnace (Gallenkamp muffle furnace size 2) in air, according to the thermal debinding cycle designed from the TGA results (discussed in section 5.2.1).

The TGA results indicate the required debinding temperature for thermal decomposition of the space holder and binder materials. The time at temperature required to ensure that all space holders and binding materials within the samples would be fully decomposed was chosen to be similar to other studies, as approximately 5 to 12 hours (Wen *et al.*, 2001 and Imwinkelried, 2007).

To verify that full debinding was complete, the mass of the brown samples measured. Once all the space holder and binder material is removed from the green sample, its mass should be equivalent to that of the mass of titanium powder

present in the sample. This comparison was used to determine the efficiency of the debinding step.

SEM, Density and Dimensional analysis

All analyses were conducted as explained in section 5.2.1.

EDS analysis

Similarly, EDS analysis, as described in section 5.2.1, was conducted on the debound and sintered samples. Three areas of importance were investigated the area nearest to the surface of the sample, the area surrounding the edges of the major pores (pores produce by the removal of ammonium bicarbonate) and finally, the core of the metallic material, between the major pores. The sample surface and major pore surfaces was analysed to determine if contamination had occurred during the debinding or sintering processes, due to reaction with the space holder or binder materials, or with the debinding or sintering atmospheres. The metallic core of the sample was analysed to determine whether surface contamination penetrated deep into the material.

5.2.6. Sintering

Sintering was conducted in a horizontal tube furnace (make: Elite, model: TSH 15-50-180) under vacuum. Before sintering, a low vacuum of 10^{-2} mbar is pulled using a rotary vane pump (make: Adixen, model: Pascal 2012 SD). The furnace chamber, the tube, is then flushed with ultra-high purity (UHP) argon (supplier: AFROX). This is done to assist in the removal of all oxygen from the furnace before the final high vacuum of 10^{-6} mbar is pulled using a turbo pump (make: Varian model: Turbo-V 81-M). The heating cycle begins after at least 10^{-5} mbar vacuum is reached in order to ensure that no low temperature reaction with any residual oxygen or nitrogen in the furnace atmosphere occurs. Once the sintering cycle is complete, the furnace goes into a cooling cycle where the induction element is switched off and the furnace is allowed to cool while still under high vacuum. Only when the furnace temperature drops below 500 ºC is argon slowly flushed back into the furnace into the furnace to assist in the cooling cycle. The argon flushing also assists in cooling of the turbo pump and rotary pump.

The above sintering procedure was designed to safe guard the equipment from being damage as well as preventing contamination from occurring within the samples. It was crucial that the correct furnace operation procedures are followed as the equipment is fragile and will be damaged if the turbo pump is switch on before an initial low vacuum of $5x10^{-2}$ torr is achieved. Likewise the equipment will be damaged if the vacuum system is exposed to pressures exceeding atmospheric pressure, if the heating cycles required temperature increase is too great or if the dwell temperature is too high.

Samples were sintered in yttria-doped zirconia crucibles which can withstand temperatures of up to 1500 ˚C and is commonly used when sintering titanium.

Three-point bending test

A three-point bending test, rather than compression or tensile test, was conducted on all samples for multiple reasons: the typical loading conditions of implants are better simulated by three point bending tests which simulate a combined tension/compression stress state, the samples' geometry is not suitable for accurate tensile or compression testing, the foams would be crushed at the clamping locations for tensile testing, and finally, three-point bending tests are frequently used for mechanical testing of sintered material.

The three-point bending test was conducted according to (ASTM Standard B528, 2005) standards using a mechanical testing machine (load frame: MTS Criterion 43, force transducer: 30 kN serial 220409 Kraftaufnehemer force transducer). A transverse rupture strength fixture, as shown in Figure 11, was used to support the bar between two, raised ∅3 mm rods, 25 mm apart, while a load was applied midway between the supports by a similar rod. The MTS criterion is regularly calibrated and has a load and position accuracy of ±0.5%. The data is captured using the supplied machine software which caters for the mechanical response and behaviours of the load frame and adjust captured data accordingly.

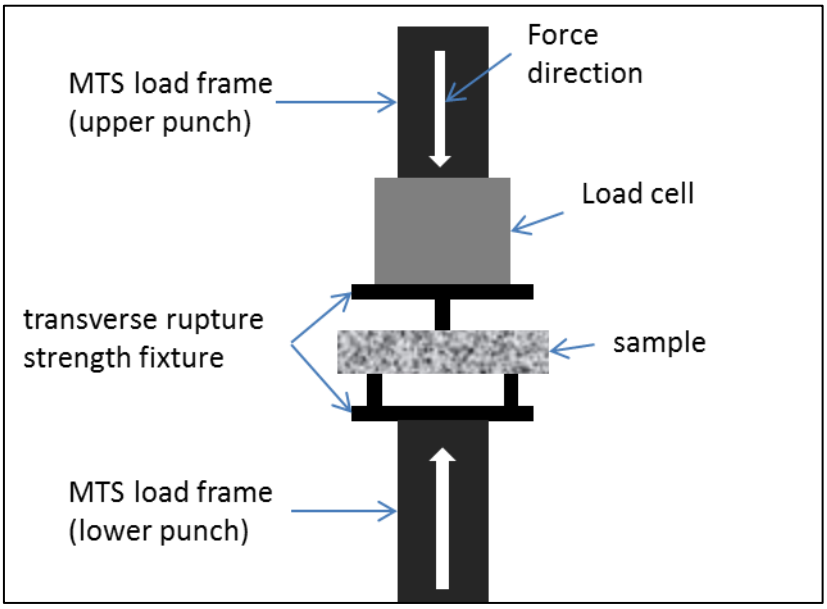

Figure 11: Figure of three point bending setup

The displacement and force was measured via the load frame's internal displacement and force transducers and captured on a linked computer (Dell). The displacement rate of the lower platen during testing was 1 mm/min with a data capture rate of 5 data points per second.

The flexural stress of the samples is determined using the following equation (ASTM Standard B528, 2005):

$$\sigma = \frac{3 \times P \times L}{2 \times t^2 \times w} \quad (12)$$

where

σ = maximum stress within specimen, MPa,
P = force exerted onto sample, N,
L = distance between the fixtures lower two prongs, mm,
t = thickness of sample, mm,
w = width of sample, mm.

The transverse rupture strength of the material is taken as the maximum value of flexural stress, as calculated from equation (12). Young's modulus is determined by rearranging the deflection equation for a simply supported beam with a midlength load (Ashby, et al., 2000). To ensure that the equation is only used within the linear elastic region, only the initial linear stress-strain curve data was used to compute Young's modulus. The average was determined by taking a rolling average and was reported. The initial linear area was determined by linear regression over the initial selection and chosen over the area with minimal deviation.

$$E = \frac{PL^3}{3 \times \delta \times t^3 \times w} \quad (13)$$

where

P = force exerted onto sample, N,
L = distance between the fixtures lower two prongs, mm,
δ = deflection of midpoint, mm,
t = thickness of sample, mm,
w = width of sample, mm.

Light Microscopy

Light microscopy was used to analyse the microstructures of the sintered samples using an inverted metallurgical microscope (make: Olympus, model: GX51). The specimens were mounted in an epoxy resin under vacuum to ensure the epoxy fills up all cavities. This was done to ensure the structural integrity of the pores remained during the grinding and polishing stage. The grinding and polishing was done in accordance to documentation prepared by Struers (Taylor & Weidmann, 2008).

Micrographs of the samples were captured digitally (Olympus Streamline) and processed using ImageJ, an open source imaging programme, in order to determine the pore characteristics, such as average pore size and pore size distribution. Both of these characteristics were determined through 2D analysis of the pore characteristics, more commonly referred to as quantitative image analysis (Wen, et al., 2001). This type of analysis is common practise in microstructural analysis and typically requires large number of data points to give a relatively good estimate of the pore size distribution in the material. The quantitative image analysis technique used in this study is described in Appendix C. It is assumed

that the accuracy of this 2D measurement technique suffices for this research; it yields enough information to allow satisfactory interpretation of the microstructures and the influences of the processing parameters on the microstructures, and is relatively computationally inexpensive.

6. RESULTS

This section entails aspects relevant to the conduction and outcome of all steps within the experimental procedure. Results are shown sequentially according to Figure 9, within section 5.2.

6.1. Production selection

6.1.1. SEM imaging of titanium powder and ammonium bicarbonate

The SEM analysis was conducted to determine the powder size and shape characteristics of both the titanium powders and ammonium bicarbonate powders. The SEM images are shown in Figure 12 to Figure 16.

Figure 12 and Figure 13 show the AA powder at high and low magnifications, respectively. The TiAA powder is observed to be angular and have an average particle size of 30 – 40 µm.

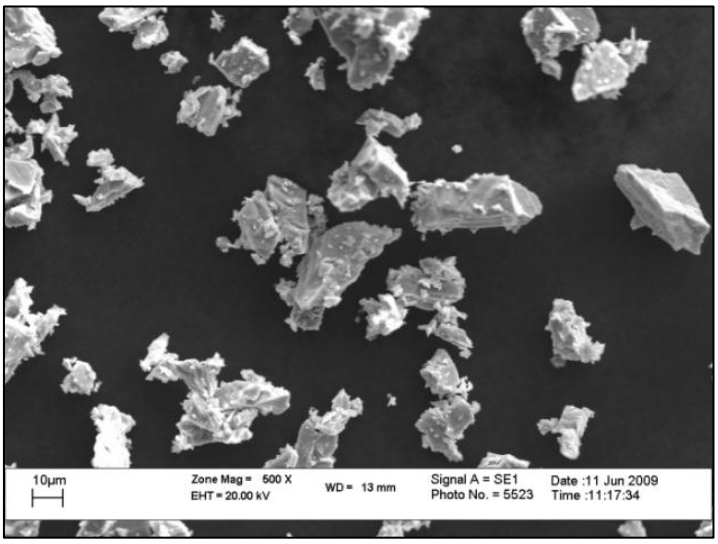

Figure 12: SEM of TiAA powder at high magnification

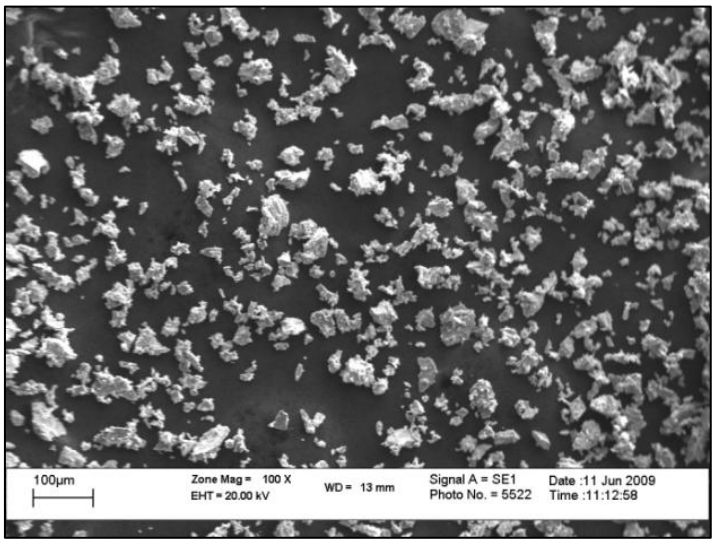

Figure 13: SEM of TiAA powder at low magnification

Figure 14 and Figure 15 show the TiG powders at high and low magnifications, respectively. The G is observed to be angular and have an average particle size of 60-80 µm.

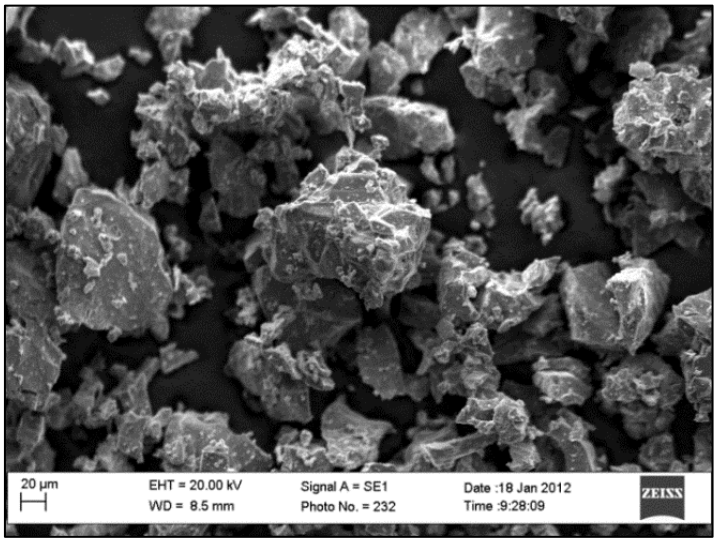

Figure 14: SEM of TiG powder at high magnification

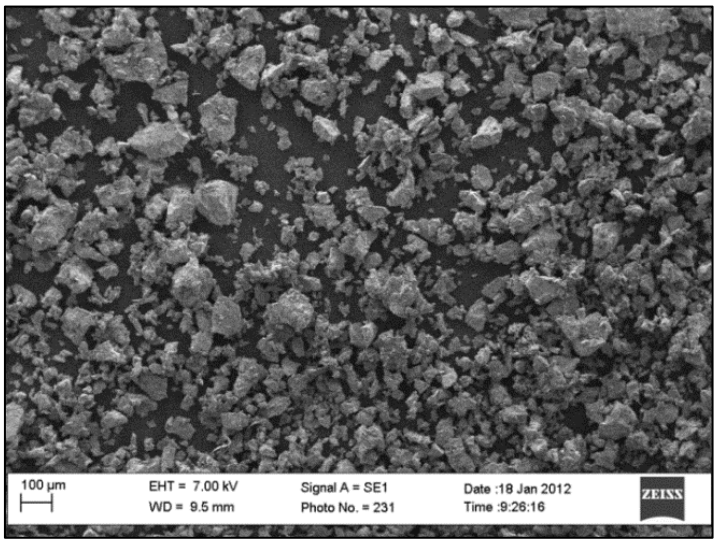

Figure 15: SEM of TiG powder at low magnification

Figure 16 shows the ammonium bicarbonate powder at low magnifications. The powders were observed to be prismatic with particles size in the range of 100-500 µm.

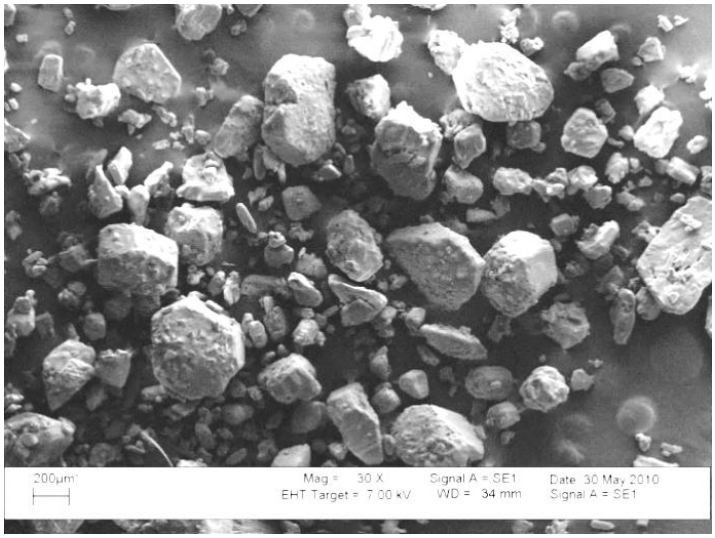

Figure 16: SEM of ammonium bicarbonate at low magnification

From these figures it is apparent that the ammonium bicarbonate particle size is approximately 6-7 times larger than that of the titanium powder. This size difference allowed the titanium powder to completely surround the ammonium bicarbonate particles and for the titanium powder particles to mechanically bond together during compaction so as to give the green samples enough strength for handling. This is required in order to form mechanically rigid foams. This interconnected network of titanium powder particles is crucial for sintering, where sufficient titanium powder particles will be in contact with each other, allowing

interparticle sinter bond necks to form. Eventually, after the titanium powder particles have fully sintered together, the continuous skeletal structure of the titanium foam is all that will remain.

6.1.2. Particle size analysis

Particle size distribution was measured using laser diffraction as explained in section 5.2.1. The particles were suspended in isopropanol and sonicated for 60 sec before the analysis. A flow rate of 12 *L/min* and a refractive index of 1.376 was used for the analysis. Figure 18 and Figure 17 show the particle size distribution as measured for the TiG and TiAA powders, respectively. It is reported by volume frequency versus diameter.

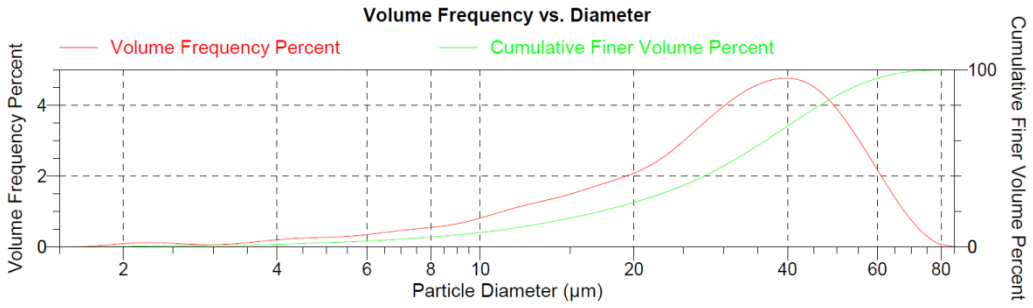

Figure 17: Particle size distribution of TiAA powder

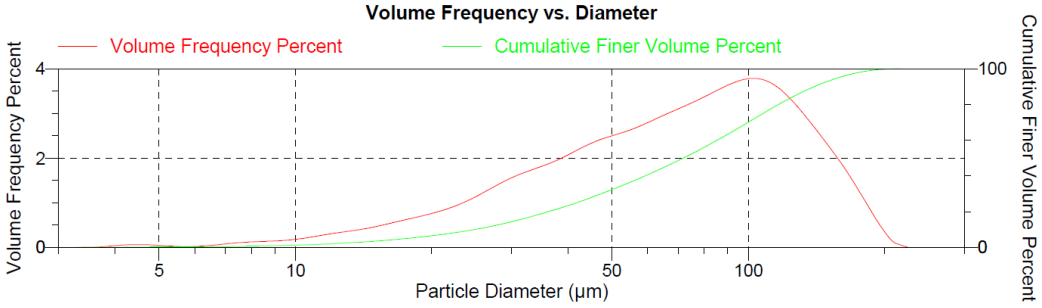

Figure 18: Particle size distribution of TiG powder

Table 4 summarises the particle size distribution, reporting the mean, median and D50 particle sizes ± 3 standard deviations (3SD). The D50 particle size indicates the particle size for which 50 vol% of the particles are smaller.

Table 4: Particle size analysis results from laser diffraction

Powder	Mean (µm) ± 3SD(µm)	Median (µm) ± 3SD(µm)	D50 Particle Size (µm)
TiAA	32.3 ± 0.2	31.8 ± 0.2	31.8
TiG	77.6 ± 0.3	77.6 ± 0.2	71.8

6.1.3. TGA of ammonium bicarbonate and PEG

TGA analysis was conducted to determine the thermal degradation characteristics of both PEG and ammonium bicarbonate. The analysis was conducted in both an inert atmosphere (argon) and normal atmosphere (air). The results of this analysis are depicted in Figure 19 to Figure 22. The optimum temperature for degradation was determined by taking the derivative of mass percentage with respect to temperature.

Figure 19 and Figure 20 depict the thermal degradation of PEG in air and argon, respectively. The temperature at which the peak rate of thermal degradation is observed is approximately 300-330 ˚C in air and 400-420 ˚C in argon. This 100 ˚C difference is largely due to the presence of oxygen in air.

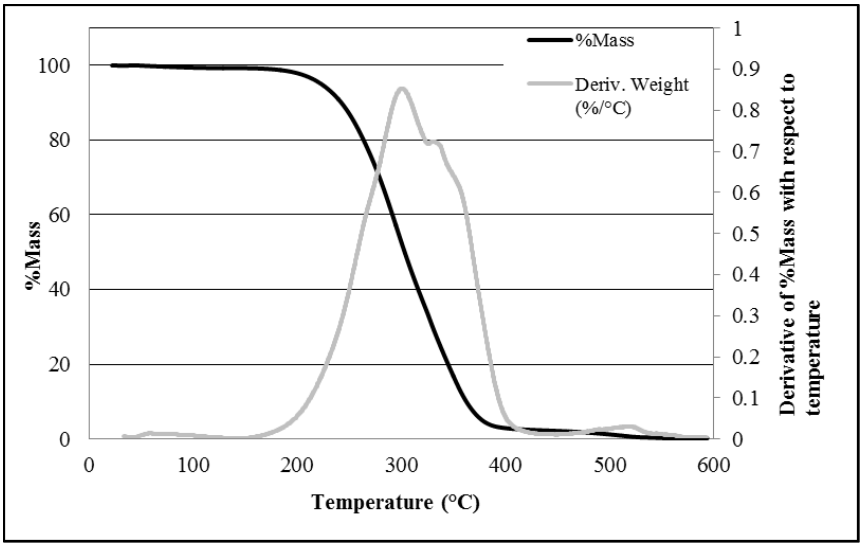

Figure 19: Thermal degradation of PEG in air

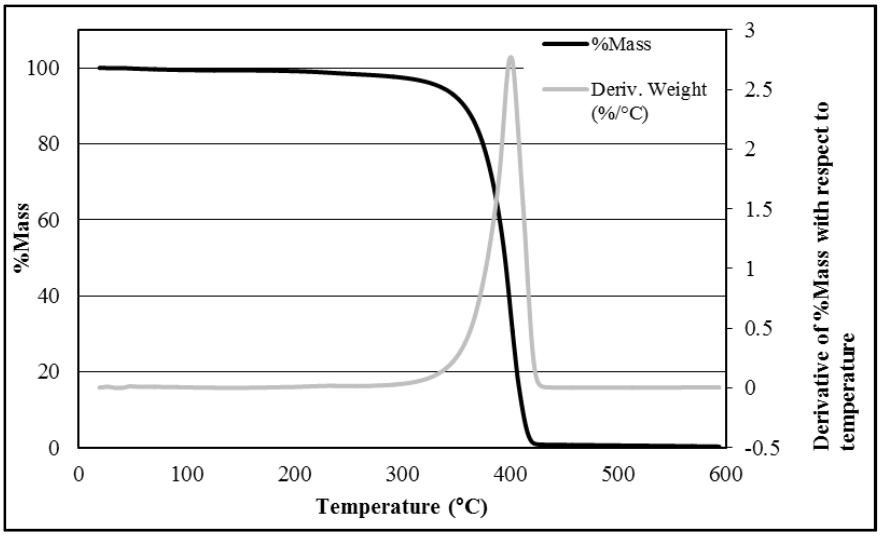

Figure 20: Thermal degradation of PEG in argon

Figure 21 and Figure 22 depict the thermal degradation of ammonium bicarbonate in air and argon, respectively. The temperature at which the peak rate of thermal degradation occurs is approximately 100-140 ˚C for both atmospheres. This is due to ammonium bicarbonate being an unstable compound, which decomposes into ammonia, water and carbon dioxide when in the presence of air (Bram, et al., 2006). As all elements are bonded fairly weakly within the compound, only small amount of heat is required for decomposition to occur, typically decomposition occurs at temperatures in excess of 41.9 ºC in the presence of air (Bram, et al., 2006).

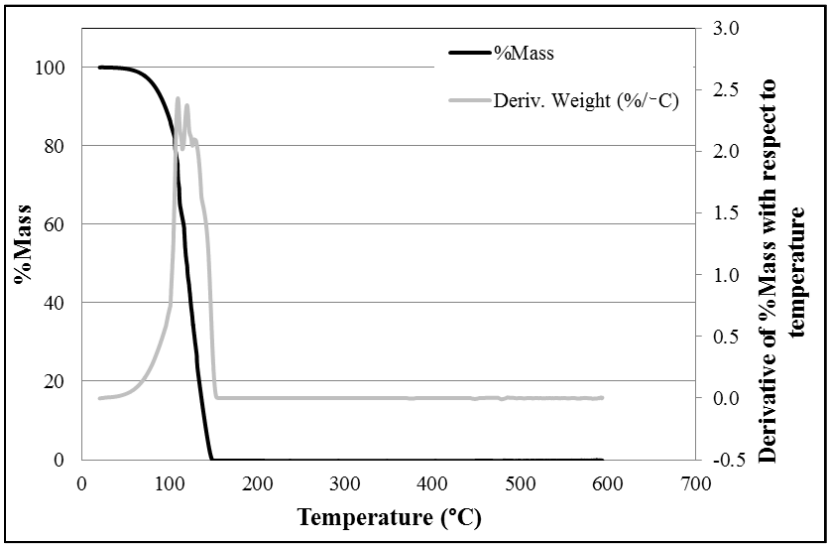

Figure 21: Thermal degradation of ammonium bicarbonate in air

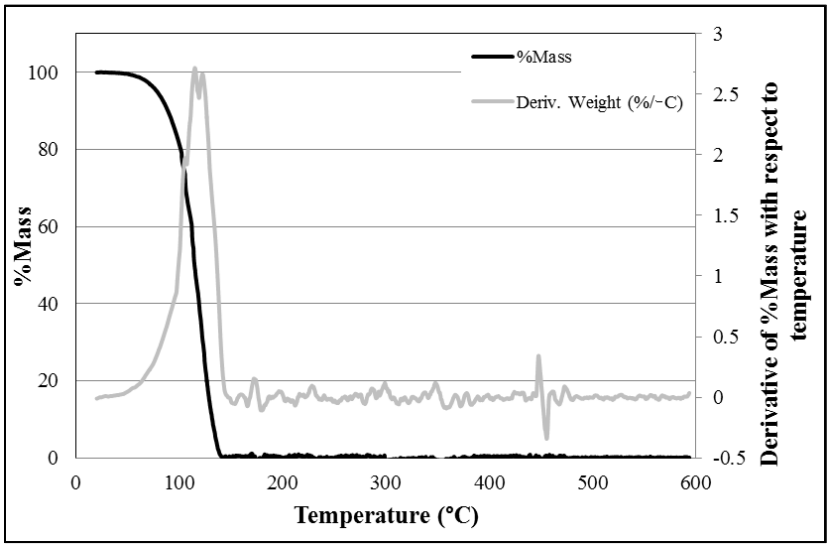

Figure 22: Thermal degradation of ammonium bicarbonate in argon

The oxidisation behaviour of both titanium powders was evaluated by TGA. The analysis was conducted under normal atmosphere (air). The results of this analysis are depicted in Figure 23.

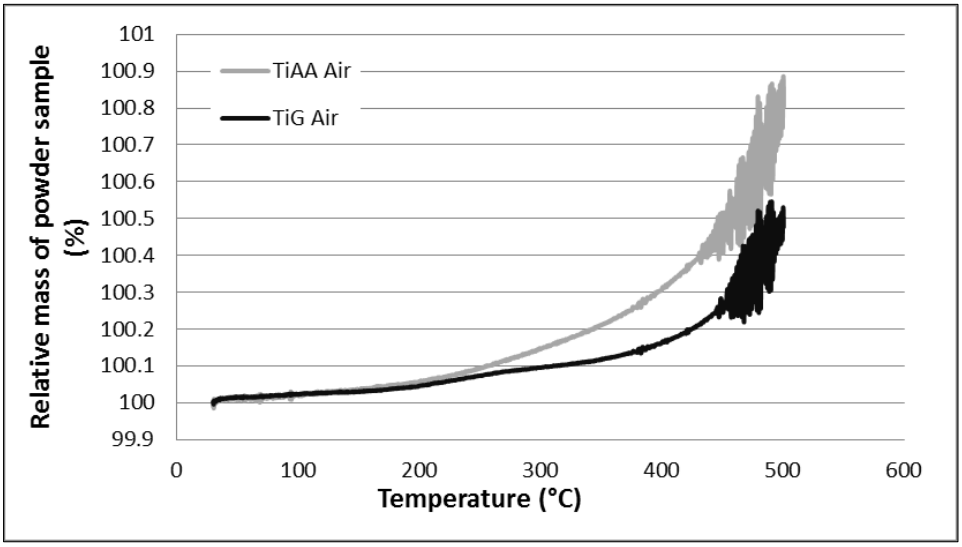

Figure 23: Oxidisation behaviour of titanium powders in air

From Figure 23, it is important to note the difference in behaviour between the TiAA and the TiG powder. This difference is largely due to the different morphology and particle size of the powders. As is reported in section 6.1.1 and 6.1.2, the TiAA powder has a smaller particle size and therefore a higher surface area to volume ratio than that of the TiG. This larger surface area allows the powder to oxidise and therefore pick up mass more rapidly.

From Figure 23 it is evident that the critical oxidation temperature, the temperature at which the rate of oxidation starts to rapidly increase, for TiAA is just above 300 ºC and for TiG it is just above 400 ºC, determined by linear regression.

6.1.4. EDS analysis

Energy dispersive spectroscopy (EDS) analysis was conducted on both the TiG and TiAA powder, during the SEM analysis. No oxygen or nitrogen was detected on the as-received powder. This result supports the as-supplied specifications for the titanium powders: commercial pure, grade 3 (ASTM Standard F1580, 2001).

Table 5: Results of EDS analysis conducted on sintered samples

	Weight% N	Weight% O	Weight% Ti
TiG	0	0	100
TiAA	0	0	100

It should, however, be noted that EDS is not a highly accurate chemical analysis technique. EDS accuracy is typically 2 % relative error. This is largely due to the factors of uncertainties in the composition of the standards and errors in the various corrections which need to be applied to the raw data (B.K, 1991).

6.2. Sieving

The sieving procedure is outlined in section 5.2.2. Post sieving the majority of powder was found to fall between the 250-425 µm particle ranges, with small amounts of powder passing through the 108 µm sieves. All ranges where taken and stored separately in airtight containers.

6.3. Mixing

6.3.1. Mass of mixture constituents

The mixture constituent ratio was determined as explained in and Appendix A. 100 g of powder mixture was sufficient to produce all the required samples for each mixture. Table 6 gives the mixture constituent ratio, in both mass and volume percentage (assuming a 30 vol% as explained in section 5.2.3), along with the constituent mass required for a 100 g of mixture.

Table 6: Mixture constituent ratio and masses

	Mass per batch (g)	fraction of mixture	
		(wt%)	(vol%)
Titanium	57.15	57.15	22.20
Ammonium bicarbonate	41.40	41.40	45.80
Polyethylene glycol	1.45	1.45	2.00
Void fraction	-	-	30.00
Total	100	100	100.00

6.3.2. Mixing of constituencies

For the mixing of the constituents, each constituent was weighed and added to the batch, as explain in Section 5.2.3. Note: to investigate the effects of varying the space holder particle size distribution had on the final material, the different sieved ABC particle size batches where mixed in the same ratio by weight for each mixture batch. Table 7, shows the different titanium powder and space holder particle sizes used to create each batch.

Table 7: Particle size designations

Space Holder particle size (µm)	Name of mixture using TiAA as the base metal	Name of mixture using TiG as the base metal
0 – 710	AA 0 - 710	-
250- 425	AA 250 - 425	G 250 - 425
425 - 560	AA 425 - 560	G 425 - 560
560 – 725	-	G 560 - 710

6.3.3. Apparent density analysis

The apparent density analysis was conducted in accordance to section 5.2.3. It was found that after mixing for 10 min, at 60 rpm, in 3D turbula-like powder mixer the powder mixture was homogenous. Table 8 shows the apparent density analysis conducted on mixtures AA 0 – 750 and G 250-425.

Table 8: Results of the apparent density analysis conducted on the mixtures

	AA 0 – 750 µm		G 250-425 µm	
Apparent density measurements	Apparent density (g/cm^3)	Variance from Average (%)	Apparent density (g/cm^3)	Variance from Average (%)
1	1.18	0.02	1.18	0.08
2	1.18	0.05	1.18	0.02
3	1.18	0.07	1.18	0.10
Average	1.18	0.05	1.18	0.07

From Table 8 it is visible that the mixtures were homogeneously mixed. This is largely due to the variance in apparent density between samples being relatively small, typically below 0.5 % variance.

6.4. Compaction

As mentioned in section 5.2.4, all specimens where uniaxially compressed at 100 MPa using 5 g per sample for each of the different of mixtures, see Table 7.

6.4.1. Compaction of samples

It was initially planned to produce 10 samples for each mixture: 3 samples would be used to determine the green strength, 1 sample to determine the brown strength, 3 sintered samples to determine the sintered strength, microscopy and SEM, and the remaining 3 sintered samples would serve as backups for unforeseen circumstances. For every 10 samples produced for in a set, 7 samples were debound and of these, only 6 samples were sintered.

After testing the strength of the green and brown samples of the first few sets, it became evident that these values were very low and difficult to measure accurately. The green and brown strengths typically ranged between 1.5 - 4.5 MPa. Accordingly, samples for these tests were omitted from further sets.

Therefore, it was decided that for the subsequent sets only 8 samples were required per set. Of the 8 samples, 7 samples were debound and 6 sintered. These samples where then used to conduct light microscopy, density and SEM analysis for green, brown and sintered states. The three-point bending test was only conducted for sintered samples for these sets.

Figure 24: Green sample from mixture AA 0-710

Figure 24 shows a photo of a green sample produced. As seen in Figure 24, there are no visible pores. This is due to the ammonium bicarbonate and PEG still filling the pores.

6.4.2. Dimensional analysis

As explained in section 5.2.4, the sample's dimensions at each process step were recorded. As expected, straight after compaction the average dimensional size of the samples remained fairly constant. It was found that the average samples dimensions were 31.90 mm in length, 12.74 mm in width, and 6.39 mm in thickness for TiAA and 6.46 mm in thickness for TiG with each having standard deviation of ± 0.02 mm. This thickness difference was expected as the TiAA powder has a smaller particle size than that of the TiG and this correlates to less TiAA powder compacted better than its counterpart.

6.4.3. Density analysis

The density analysis of the green compacts was determined from the compact dimensions and the mass. The average calculated density of the samples was 1.90 ± 0.08 g/cm^3 for TiG and 1.86 ± 0.09 g/cm^3 for TiAA, independent of the size of ammonium bicarbonate space holder powder used.

6.4.4. SEM analysis

An SEM analysis was conducted on an AA 0 - 710 green specimen. The analysis was conducted to determine how the titanium particles pack around the ammonium bicarbonate particles. As seen in Figure 25, most of the ammonium bicarbonate had already decomposed prior to the actual analysis being done. This was due to the time elapsed between the mount, polishing and SEM imaging being done; note the no vacuum was pulled for this mounting so that the internal structure becomes visible.

It is evident that the ammonium bicarbonate produces large elliptical shaped pores after decomposing. It is also visible that the titanium powder is able to flow and pack sufficiently around the ammonium bicarbonate particles in order to create a connected metal skeleton structure. This provides the mechanical strength of the specimen.

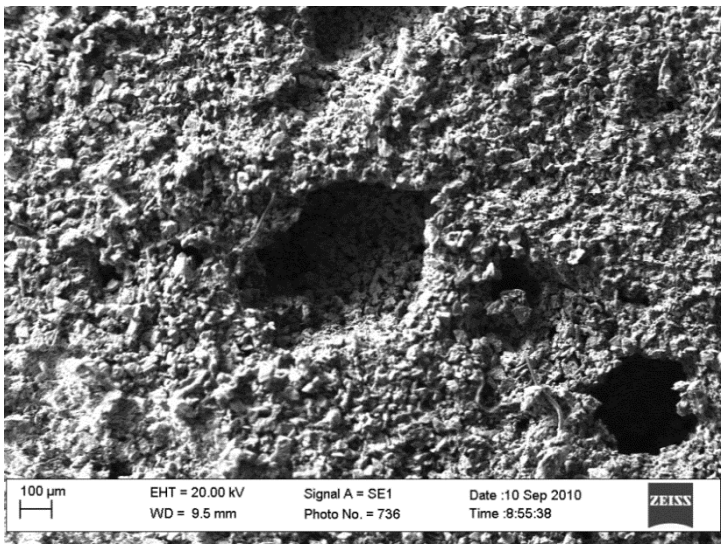

Figure 25 : SEM image of green sample from mixture AA 0-710

6.5. Debinding

Debinding was conducted in accordance to section 5.2.5, with the debinding temperature cycle based on the TGA results given in section 6.1.3 and 6.1.4. Figure 26 shows the debinding temperature profile used to ensure all ammonium bicarbonate and PEG were removed without allowing the titanium powder to oxidise too much.

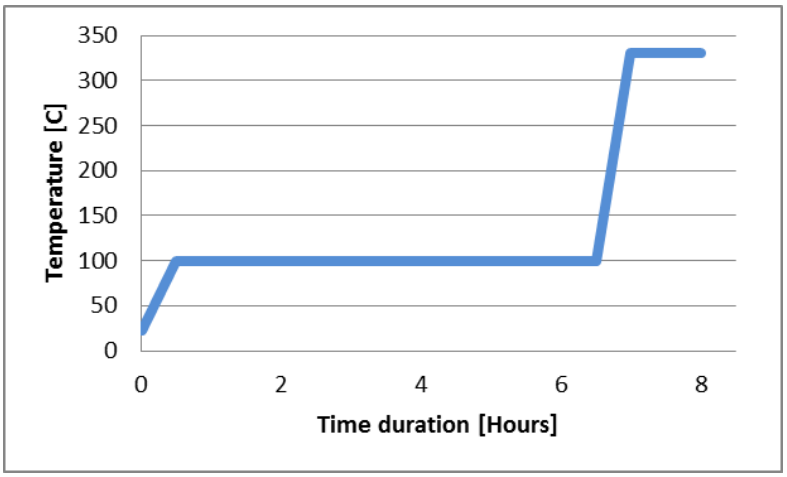

Figure 26: Debinding temperature profile

The initial heat up rate from standard atmospheric conditions was set at 3 ˚C/min. This rate was assumed to be low enough so that the vaporization rate of the ammonium bicarbonate would be slow enough not to result in internal pressure build-up. Any internal build-up of pressure could damage the samples, as the samples are very brittle and lightly compacted.

The first set-point temperature was 100 ˚C, where the samples were held for 6 hours. This temperature was chosen as the optimum temperature for decomposition of ammonium bicarbonate is between 100-140 ˚C. As PEG decomposes at temperatures of 300-330 ˚C, the second temperature set-point was set to 330 ˚C, where the samples were held for 1 hour. Thereafter the samples were allowed to furnace cool until a temperature of 50 ˚C. This cooling process took an addition 6 hours.

To determine whether all PEG and ABC were removed successfully, the brown samples' mass was compared to the expected mass of the titanium powder in each green sample. For all the specimens weighed, the mass of the brown sample corresponded to that of the expected mass of titanium powder in each green sample, within ±0.01 g. This confirmed that the debinding process was successful, and that all PEG and ABC were removed from the samples. It should be noted that the expected mass of titanium powder in each green sample is based on the assumption that each mixture was homogeneous and that, therefore, each green sample contained the exact same mass of titanium powder.

The entire debinding cycle took place in air. TGA of the titanium powders, TiAA and TiG, showed < 0.2 % and < 0.1 % increase in mass, respectively, during constant heating in air by 330 ºC. This indicates that there is potential for oxidation of the titanium powders during debinding at 330 ºC, and even more so when holding at this temperature for an hour. However, 0.2 % increase in mass due to oxidation of the titanium powder in one 5 g sample corresponds to 0.006 g. Therefore, it was assumed that oxidation of the green sample during debinding was negligible and could be omitted from consideration in weighing the samples before and after debinding.

Figure 27: Brown sample from mixture AA 0-710

Figure 27 shows a photo of a brown sample. As seen in Figure 27, there are visible pores connected to the sample surface. This is due to the ammonium bicarbonate and PEG that has burnt off and left large pores in the sample. It is interesting to note the slight gold colour change which takes place during the debinding stage. This is due to the small amount of oxidation which occurs during the debinding of the PEG.

6.5.1. SEM

Figure 28 is a SEM micrograph of a brown AA 0-710 sample. From the micrograph it is visible that very little to no sintering occurred during debinding. This is to be expected as the debinding temperature was chosen to be far below the sintering temperature. Compared to the SEM image, Figure 25, of the green sample, the surface of the space holder macropores is not as smooth. This is assumed to be due to all the ammonium bicarbonate being successfully removed from the pores.

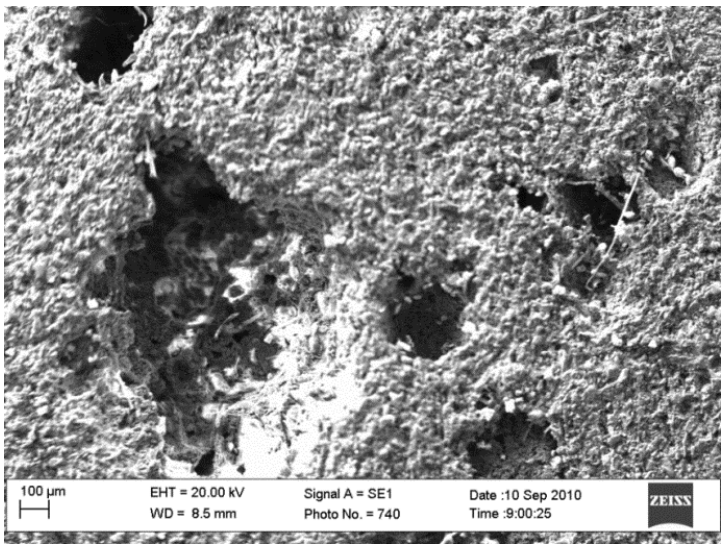

Figure 28: SEM image of a brown sample from AA 0-710 mixture

6.6. Sintering

The samples were sintered in accordance to section 5.2.6. All the specimens were sintered under high vacuum at 1200 ˚C for 2 hours, with heating and cooling rates of 5 ˚C per minute on an Yttria-doped zirconia substrate, crucibles show in Figure 29.

Figure 29: Yttria-doped zirconia crucible

Figure 30: Sintered sample from AA 0-710 mixture

Figure 30 shows a sintered sample. The colour of the sample is silvery-grey, similar to that which is to be expected of pure titanium. This indicates that the vacuum, and possibly the alumina tube, helped to reduce surface oxidation that occurred during debinding. Note that the brown samples showed a golden tint after debinding, which is an indication of titanium oxide.

6.6.1. EDS

An EDS analysis was conducted on the sintered specimens according to section 5.2.5. Multiple measurements were taken at region around large pores, at the core of the samples and near the external surface. The measurements around the pores edges were taking as close to the pore edge as possible, the core measurement were taken in regions as far away from either macro- or micropores as possible. The surface measurements were taken as close to the external surface of the sample.

Table 9: Results of EDS analysis conducted on sintered sample

	Weight% N	Weight% O	Weight% Ti
Pore	0	8	85
Core	0	2	91
Surface	0	3	95

Table 9 shows the EDS results from a sintered AA 0-710 sample. It shows that the highest level of oxidation occurred at the edge of the large pores and at the surface. This indicates that oxygen diffuses into the core of the sintered titanium.

As mentioned in the section 6.1.4, it should be noted that EDS is not a highly accurate, quantitative chemical analysis technique; typically 2 % relative error is expected in results. This is largely due to the factors of uncertainties in the composition of the standards and errors in the various corrections which need to be applied to the raw data (B.K, 1991). Therefore the reported oxygen wt% values should rather only be viewed qualitatively, in comparison to each other. As such, the analysis indicates that oxidation occurred at the pore edges and that the oxygen slowly diffuses into the solid titanium scaffolding material. However, there is evidence of a concentration gradient moving from the pore edge to core of the skeleton material.

6.6.2. Microscopy

Microstructural analysis of the sintered samples was conducted on all specimens in accordance to section 5.2.6. Figure 31, shows a SEM image of a sintered AA 0-710 sample. The pores were filled by vacuum impregnation with a fluorescent epoxy resin for light microscopy. This was done to ensure that the pores do not close during the preparation process.

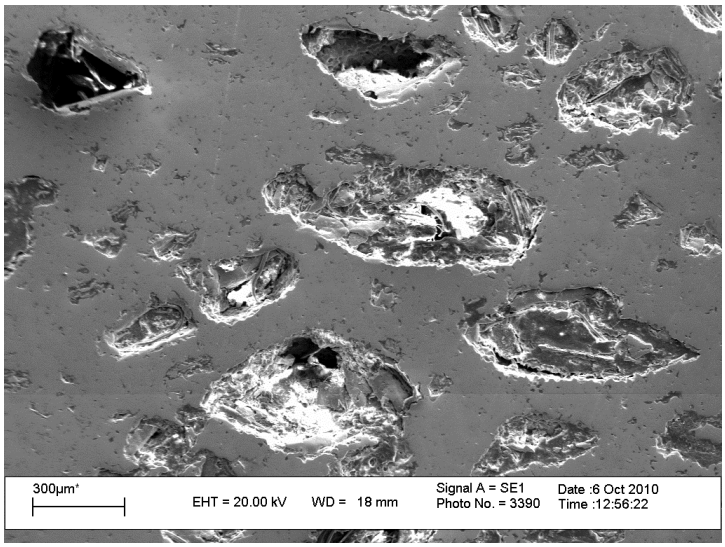

Figure 31: SEM image of a sectioned sintered sample from AA 0-710 mixture

The pores, as shown in Figure 31, are elliptical and have similar characteristics to that of the initial pores shown in Figure 25.

The micrographs in Figure 32, on page 46, show the sintered foam microstructures of the samples produced from the two different titanium powders, AA microstructures shown on the left and G on the right. The relevant information (mixture designation, porosity and average pore size) for each sample is given below each micrograph. The average pore size was determined as explained in Appendix C.

The AA mixture microstructures show a denser titanium metal network than that of the G mixture microstructures. There are fewer micropores, and they are more spherical as opposed to the irregularly shaped, sharp edges pores of the G mixtures. Additionally, the macropore foam structure, formed from each different initial space holder particle size range, develops differently for each titanium powder, AA and G. Both of these points are discussed in details, within section 7.

6.6.3. Dimensional analysis

The average dimensions of the samples for each of the mixtures, measured according to section 5.2.4, are shown in Table 10, on page 47. Table 10 shows the mean and the standard deviation of each dimension.

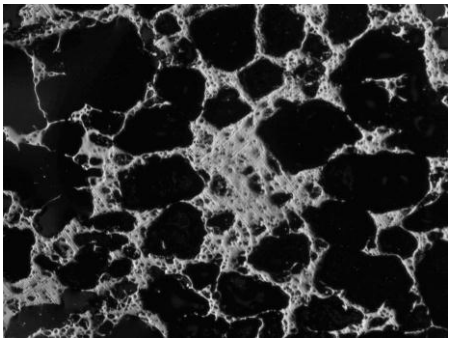

Powder mixture AA 0 - 710
61 % porosity
average pore size 285 µm

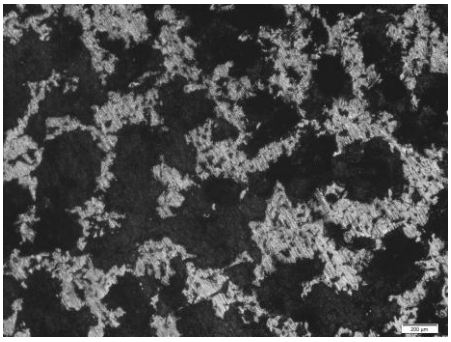

Powder mixture G 250 - 425
56 % porosity
average pore size 507 µm

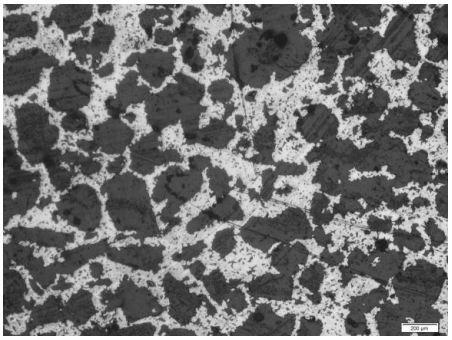

Powder mixture AA 250-425
49 % porosity
average pore size 302 µm

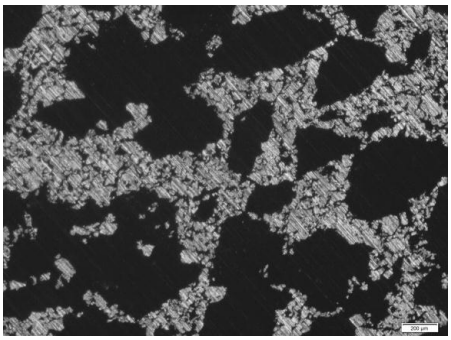

Powder mixture G 425-560
57 % porosity
average pore size 499 µm

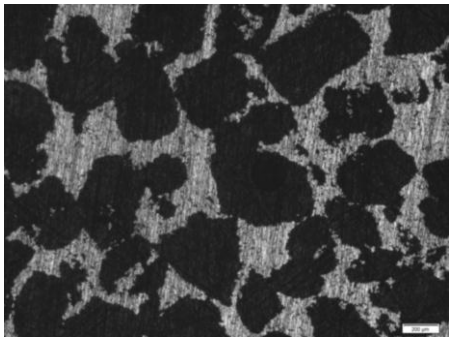

Powder mixture AA 425-560
49 % porosity
average pore size 385 µm

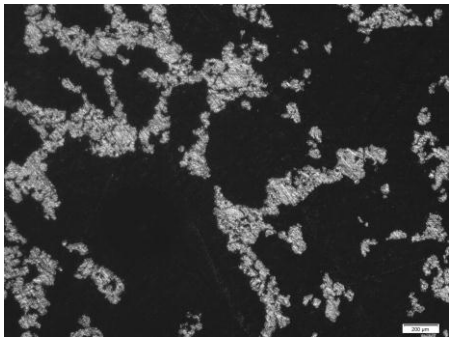

Powder mixture G 560 - 710
54 % porosity
average pore size 450 µm

Figure 32: Micrographs of the sintered titanium foams, as labelled

Table 10: Final sintered dimensions of samples, mean with standard deviation,

Initial space holder particle size	Length	Width	Thickness
AA 0-710	27.77 ± 0.11 µm	11.09 ± 0.08 µm	5.79 ± 0.04 µm
AA 250-425	27.09 ± 0.17 µm	10.80 ± 0.08 µm	5.41 ± 0.10 µm
AA 450-560	27.11 ± 0.10 µm	10.83 ± 0.04 µm	5.63 ± 0.04 µm
G 250-450	28.52 ± 0.14 µm	11.78 ± 0.12 µm	5.98 ± 0.08 µm
G 450-560	30.30 ± 0.28 µm	12.17 ± 0.18 µm	6.19 ± 0.11 µm
G 560-710	29.39 ± 0.30 µm	11.87 ± 0.04 µm	6.15 ± 0.13 µm

6.6.4. Mechanical behaviour

The transverse rupture strength and Young's modulus were determined using equations (12) and (13), with the experimental data captured in the 3-point bend test, as described in section 5.2.6. The plots of flexural stress against midpoint displacement are shown in Appendix B, Figure 42. Table 11 summarises the experimentally determined mechanical properties of the different sintered foams.

Table 11: Mechanical properties of the different titanium foams

Mixture designation	Relative density (%)	Elastic modulus (GPa)	Transverse rupture strength (MPa)
AA 0 - 710	62.5	8.4	147.2
	40.0	3.6	69.7
	37.5	2.8	56.1
AA 250 - 425	51.7	5.8	108.8
	50.3	5.3	111.1
	50.0	4.4	125.3
AA 425 - 560	51.5	5.6	101.9
	50.2	4.4	116.9
	50.1	4.7	103.8
G 250 - 425	44.0	4.2	64.9
	43.8	3.8	68.5
	43.8	2.9	68.1
	43.7	2.7	70.6
G 425 - 560	44.5	1.8	26.2
	42.8	3.0	50.8
	42.2	2.1	27.0
G 560 - 710	47.4	2.5	50.8
	46.5	2.9	65.2
	45.1	2.2	42.0

7. DISCUSSION

7.1. Powder analysis

The powder particle shape for both titanium powders, as observed in the SEM micrographs in Figure 12 to Figure 16, is angular. An angular particle shape is expected for titanium powders produced by the HDH process and occurs as a result of the crushing and milling process of the hydrogenated titanium sponge.

The particle size distribution measured by laser diffraction correlated with the size of the particles observed in the SEM micrographs. The TiAA powder is approximately half the size of the TiG powder, with mean particle sizes reported as 31.8 µm and 71.8 µm, respectively. Both powders show particle size distributions that are skewed to larger particle size. The TiAA and TiG powders were supplied as -200 (<150 µm) and -100 (<75 µm) mesh, respectively. These measurements correlate with the particle size distribution graphs shown in Figure 17 and Figure 18 where the maximum particle size measured was 80 and 150 µm, respectively. The differences between the powders' particle size distributions resulted in different behaviours throughout the manufacturing process, as will be discussed in the relevant sections to follow.

7.2. TGA analysis

The thermal decomposition characteristics of the PEG, ABC and titanium powders in air were determined from the TGA results. This information is relevant only to the debinding process, which was conducted in air. As sintering took place under high vacuum, the thermal decomposition behaviour of the powders in air was not relevant during sintering.

The TGA results, Figure 19 and Figure 21, indicate that peak thermal decomposition temperatures for PEG and ABC in air are in the range of 300-330ºC and 100-140 ºC, respectively.

The TGA of the titanium powders was conducted in order to determine whether oxidation of the titanium powders would occur if debinding was conducted in air. Both titanium powders showed significant increase in mass from temperatures above 330 ºC and 400 ºC for TiAA and TiG, respectively, which correlated to that mentioned in literature (Duncand, 2004). This indicates that oxidation of the titanium powders occurs from these temperatures. The difference in oxidation temperatures for the two powders is attributed due to the TiAA powder having a smaller particle size than of TiG. With a smaller particle size, TiAA has a higher surface area to volume ratio and thus shows significant oxidation at a lower temperature than the larger TiG powder.

These results indicate that, in order to fully debind the samples in air, it would be necessary to heat them up to at least 330 °C, the temperature at which PEG decomposes in air. As this temperature is similar to the oxidation temperature of TiAA, this was a point of concern. However, it was decided to conduct the

debinding experiment in air as planned, and to monitor the level of oxidation in the titanium network after sintering using EDS.

The debinding thermal cycle was designed from the TGA analysis results and is shown in, Figure 26. The debinding thermal cycle was designed to minimise exposure to oxidation temperatures, while still ensuring that all polymers are fully decomposed during debinding. It would be preferable, and is recommended for future studies, to debind the samples in vacuum or in flowing argon to reduce the oxidation which occurs during debinding. However, facilities for this were not available at the time of this study. Debinding in the vacuum furnace would contaminate the furnace and vacuum system, so this was not investigated.

7.3. Compaction of samples

As explained in section 6.4.1, with the powder mixtures were uniaxially compacted at compaction pressure of 100 MPa. The compaction pressure was chosen to produce samples with high porosities (Wen, et al., 2001) but that still had well-sintered titanium skeletal structures after sintering.

The samples were compacted sufficiently to be handled without breaking and to avoid delamination on ejection from the die (delamination is cause during eject of samples due to friction with the die wall). However, the degree of compaction was only sufficient to meet these requirements and the green strength of the samples was too low to be accurately measured.

7.4. EDS analysis

EDS analysis conducted on the pure titanium powders indicated that no oxides or nitrides were present on the titanium powders. This result was expected, as both powders were supplied as commercial pure with a grade of 3 according to ASTM standard F1580-01. This means that the powder should be pure with no more than 0.18 % oxygen present.

Post sintering, the yttria-stablised crucibles displayed discolouration in the areas surrounding the sample placement. It is most likely that the crucibles acted as getters during sintering, preferentially reacting with contaminants during sintering.

The oxidation results, after debinding in air and sintering in vacuum, are reported in Table 9. It is evident that oxidation did occur during processing. While EDS does not offer accurate quantitative analysis of oxygen levels, it is clear that there is a much higher concentration of oxides at the macropore surface (~8 % oxygen) than in the interior or core of the sintering titanium network (~3 % oxygen). This range is above that which is recorded by other researchers, typically between 0.25 – 1 % (Arifvianto & Zouh, 2014), which will result in samples which are more brittle.

Contaminates can generally be introduced during sintering due to three reasons: (i) residual space holder material is still present in the sample during sintered, (ii)

the furnace itself is contaminated from deposits from previous sintering and (iii) not all atmospheric air is pulled from the furnace during sintering (Arifvianto & Zouh, 2014). However, all of these general causes are unlikely as: (i) the samples were weighed after the debinding process to ensure all space holder material is removed, (ii) the furnace which was used for sintered has only been used for titanium and (iii) the furnace was flushed with argon and a high vacuum (greater than 10^{-5} mbar) was pulled to ensure minimal atmospheric contamination.

As the higher levels of oxygen were found at the surface of the macropores, it is inferred that oxidation occurs primarily during the debinding process. The process of oxidation in the samples is assumed to occur due to the decomposition of the space holder material and then subsequent heating of the sample in order to decompose the binder. As the ABC decomposes, it releases oxygen; if this oxygen is not removed from the debinding atmosphere, it reacts with the titanium as the temperature is increased during debinding. It is necessary to increase the temperature beyond the decomposition temperature of the ABC space holder material to the temperature at which PEG, the binder, decomposes. As this temperature is relatively close to the peak oxidation temperature of the titanium powders, 330 °C, oxidation of the titanium occurs.

When looking at the different regions within a sample, the regions with the highest levels of oxidation occur at the upper surfaces of the samples and the surfaces of the macropores. The increase in oxidation with respect to the upper surfaces can be explained as the upper surface is most exposed to the surrounding air during debinding.

The presence of oxygen is due to the release of the oxygen during the decomposition of the ABC and water vapour during the decomposition of PEG. However, it is suggested that the reaction of the oxygen with the titanium only occurs at higher temperatures, as the PEG is decomposed and during sintering.

7.5. Image analysis

The image analysis discussion includes the SEM and light microscopy results of the green, brown and sintered samples.

When comparing the SEM micrographs of the three different stages; green, brown and sintered (Figure 25, Figure 28 and Figure 31, respectively) it is clearly visible that there are minimal differences between the green and brown sample's microstructure, whereas significant changes, bonding and densification, occurs during sintering. In micrographs of both the green and brown samples, the individual metal powder particles are still visible; this is largely due to the debinding temperature being far below that of sinter temperature so no bonding between particles has occurred yet. However, when looking at the sintered sample micrographs, the original powder particles are not discernible from the sintered material, indicating that the particles have fused, that sintering of the skeletal foam structure has progressed significantly.

From the micrographs shown in Figure 32, it is clear that the initial individual pore shape correlates with that of the individual space holder particle shape and size for each mixture. However, after debinding, the macropores left from the decomposition of the ABC space holder often interconnect with each other to form pores which are larger than the initial space holder particle sizes.

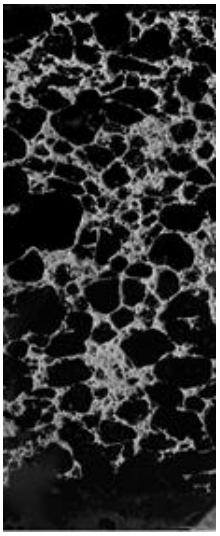

Figure 33: Pore distribution through produced samples at low magnification

Figure 33 shows a typical cross section of AA 0-710 µm sample at low magnification. The combination of both micro- and macropores that result in an open foam structure is clearly visible. The open, interconnected pores result in an open pore network which is favourable for osseointegration.

7.6. Pore size distribution

The pore size distribution was calculated by analysing the light microscopy images. ImageJ, a well know open source image analysis software, was used to determine the pore size distribution according to the techniques described in Appendix C.

7.6.1. Macropore size distribution

Table 12 gives a summary of the results found for pores which are greater than 108 µm in diameter. The particle sizes were binned according the initial ISO sieving sizes standard mentioned in section 5.2.2. These bins were selected to illustrate how the pore size distribution changes throughout the production cycle. The data in Table 12 represent the results gathered from 3 different samples per space holder particle range mixture, with 3 micrographs from different regions for each sample analysed. The pore size distribution is based on the percentage of pores found within the different bins based on the initial space holder particle size of the specific mixture.

Table 12: Macropore size distribution for each mixture

Mixture designation	% of pores <150 µm	% of pores 150-180 µm	% of pores 180 - 250 µm	% of pores 250 - 425 µm	%of pores 425-560 µm	%of pores 560 - 710 µm	%of pores >710 µm
AA 0-710	15.38	23.08	15.38	30.77	0.00	7.69	7.69
AA 250-425	24.83	18.62	24.83	13.79	6.21	2.76	8.97
AA 425-560	18.18	9.09	15.15	34.85	7.58	3.03	12.12
G 250-425	26.47	8.82	14.71	20.59	2.94	5.88	20.59
G 425-560	10.87	10.87	21.74	15.22	13.04	4.35	23.91
G 560-710	7.46	16.42	14.93	31.34	8.96	5.97	14.93

Figure 34 is a visual representation of the data presented in Table 12. A bimodal pore is clearly apparent in the sintered foams, as is shown in Figure 34. The first mode is typically at a pore size similar to the particle size of the initial space holder, however, the second mode is observed at a pore size much larger than the initial space holder particle size.

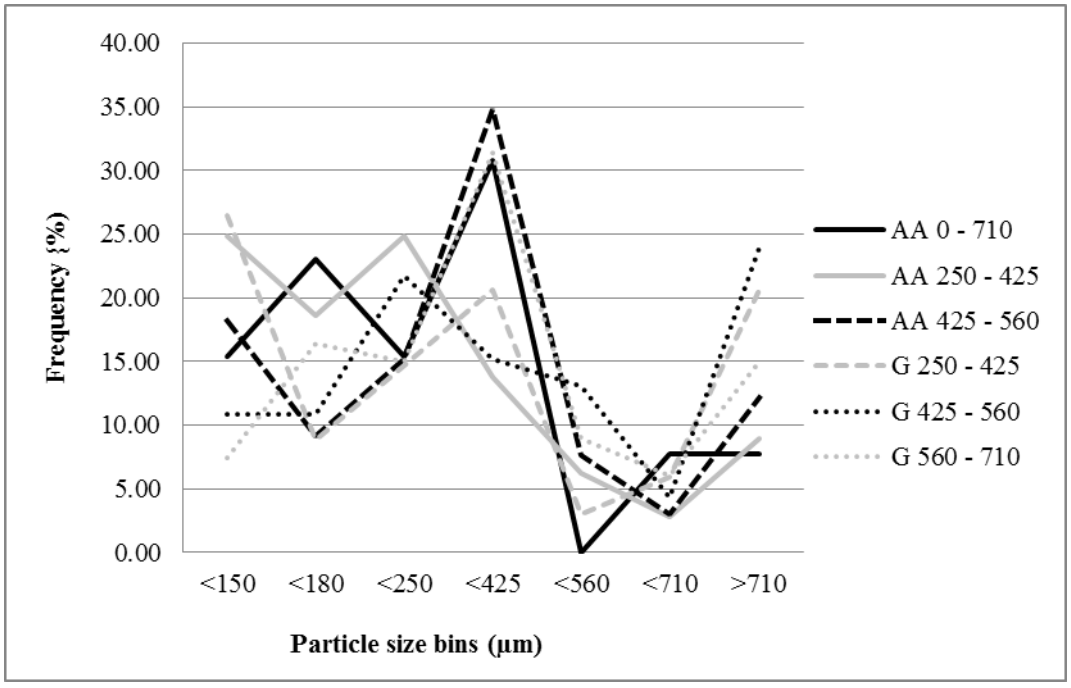

Figure 34: Macropore size distribution based on initial space holder particle size

The first macropore mode is attributed to isolated, individual macropores that have not made contact with other pores. These macropores are typical slightly smaller than the initial space holder particle size. This is attributed shrinkage during sintering, discussed more fully in section 7.7.

The second macropore mode is attributed to the interconnectivity of the individual macropores. These resultant interconnected pores form macropores which are typically much larger than the initial space holder particle size.

7.6.2. Micropore size distribution

Table 13 is similar to Table 12, except it summarises the results for pores that are less than 108 µm in diameter, the micropores.

Table 13: Micropore size distribution for each mixture studied

Mixture designation	% of pores <10 µm	% of pores <25 µm	% of pores <50 µm	% of pores <180 µm
AA 0 - 710	44.75	45.03	6.35	3.87
AA 250 - 425	51.53	37.64	8.70	2.13
AA 425 - 560	67.65	19.00	6.33	7.01
G 250 - 425	46.83	39.31	10.63	3.22
G 425 - 560	42.34	40.04	13.23	4.39
G 560 - 710	42.18	40.86	13.22	3.75

Figure 35 is a visual representation of the data presented in Table 13. From Figure 35, it is apparent that the majority of the micropores are smaller than 25 µm. Except for AA 425-560, the initial space holder particle size seems to have minimal effect on the microspore size distribution. The finer powder, AA, results in more smaller pores than the coarser powder, G.

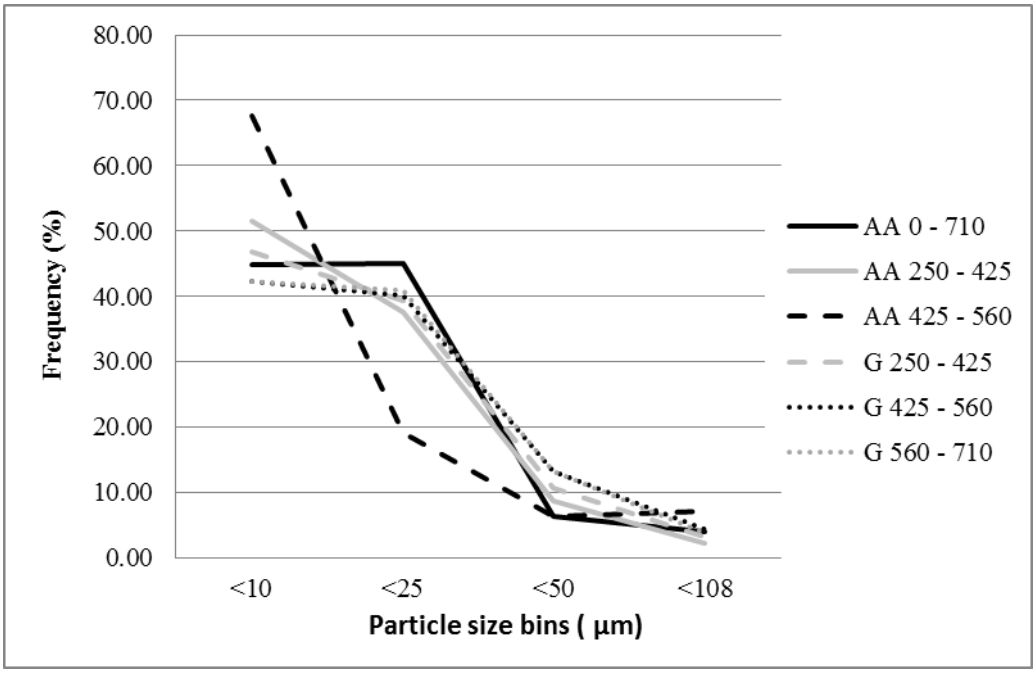

Figure 35: Micropore size distribution for each mixture studied

7.7. Dimensional analysis

There is typically a volumetric shrinkage of the material during sintering as the material densifies. The dimensions of the samples were monitored throughout all stages of the production process, in order to track the dimensional changes associated with each process step. Using equation (8) from section 5.2.4 the average dimensional changes were determined and are presented in Table 14.

Table 14: Percentage dimensional changes throughout the production process

Mixture designation	% Shrinkage in			Average shrinkage (%)
	Length (%)	Width (%)	Thickness (%)	
AA 250 - 450	15.08	15.23	15.34	15.21
AA 450 - 560	15.02	14.99	11.89	13.97
AA 0 - 710	12.95	12.95	9.39	11.76
G 250 - 450	10.60	7.54	6.42	8.18
G 450 - 560 µm	5.02	4.47	3.13	4.21
G 560 - 710 µm	7.87	6.83	3.76	6.15

The results presented in Table 11 indicate that as the particle size of the space holder powder increases, the sample shrinks less. Mentioned in section 7.6, as the particle size of the space holder powder increases, the first mode macropores, related to the space holder particle size used, also increases. Typically, the larger the pores are, the more energy is required to shrink them by sintering (German, 1996). During sintering, all samples were sintered at the same temperature for the same amount of time. As such, all the samples received the same thermal energy for sintering. Therefore, the difference in sintering shrinkage must be related to the green microstructure of the samples. It has been shown that large pores shrink at a slower rate than small pores (Pan, et al., 2009). As such, once the skeletal titanium network has sintered to near full density, any further densification of the material, and related shrinkage, happens very slowly. This explains the results shown in Table 11. Samples with smaller initial pores ultimately shrink, and densify, more than samples with larger initial pores.

The results presented in Table 11 also indicated that shrinkage is not isotropic in the samples during sintering. The shrinkage measured over the length and width of the samples are typically larger than that measured over the thickness. This is a typical sintering response of a uniaxially compacted powder where shrinkage is greater in the direction aligned with the compaction direction. This is due to the increased contact area between particles perpendicular to the compaction direction which results in a lower linear pore density, and thus a lowered potential for densification, in the transverse direction.

7.8. Mechanical properties

In general, the mechanical behaviour of the titanium foams, as summarised in Table 11 and Figure 42 in Appendix B, indicates that an increase in porosity results in a decrease of both transverse rupture strength and elastic modulus. This is in agreement with the Ashby-Gibson model as presented in section 4.5.

The proportionality constant for elastic modulus, as defined by equation (4), was found to be 0.189 for the AA mixtures and 0.136 for the G mixtures. The constant was determined through an iterative process by finding the minimum mean square error between the experimental data, Table 11, and Young's modulus as predicted by the Ashby-Gibson relationship given in equation (4). The mean square error curve is shown in Figure 36 for both the AA mixtures and G mixtures, respectively. The mean square error was calculated by determining the average of the square of the difference between the actual results and the predicted theoretical results and trying to minimise the error.

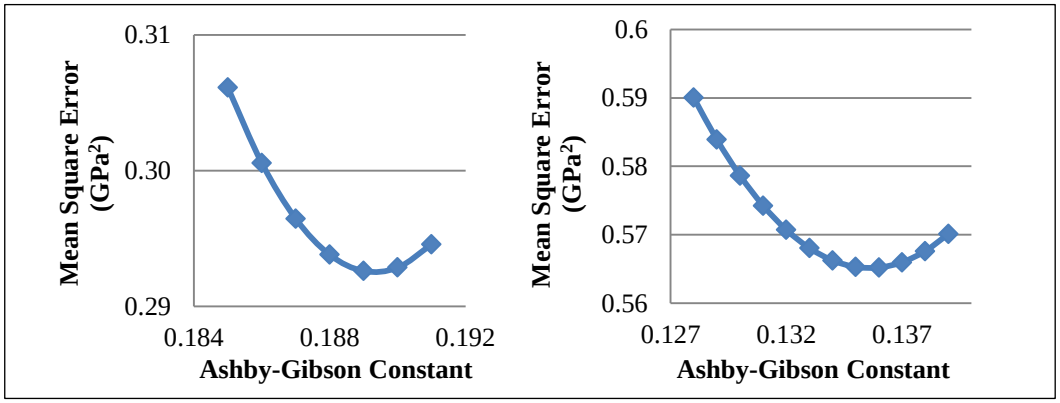

Figure 36: Mean square error curve fitting for AA (left) and G (right), for the and Ashby-Gibson elastic modulus relationship

Similarly, the model constant for the transverse rupture strength, as defined by equation (7), was found to be 0.0694 for the AA mixtures and 0.393 for the G mixtures. The variation of the mean square error with the model constant is shown in Figure 37 for the AA and G mixtures, respectively.

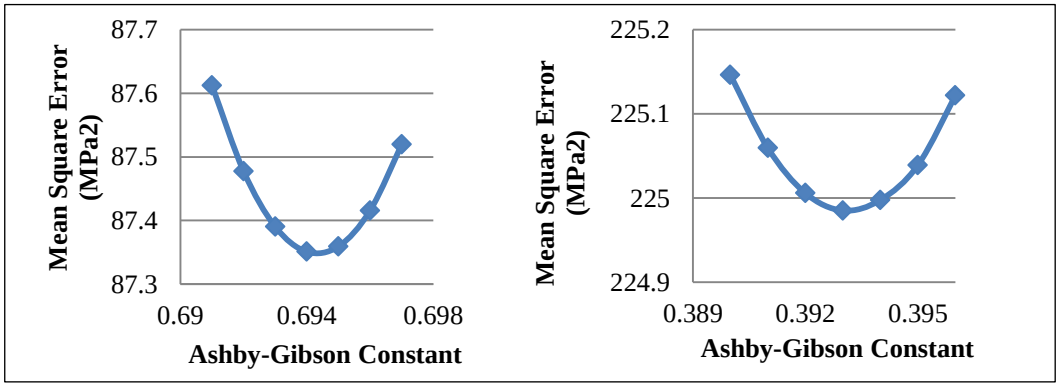

Figure 37: Mean square error curve fitting for AA (left) and G (right), for the Ashby-Gibson rupture strength relationship

Using these model constants, the Ashby-Gibson models for predicting Young's modulus and transverse rupture strength, equation (4) and (7) in section 4.5.2, are displayed in Figure 38 and 39, respectively, for both powders. The experimental data is shown for comparison as discrete data points in the figures.

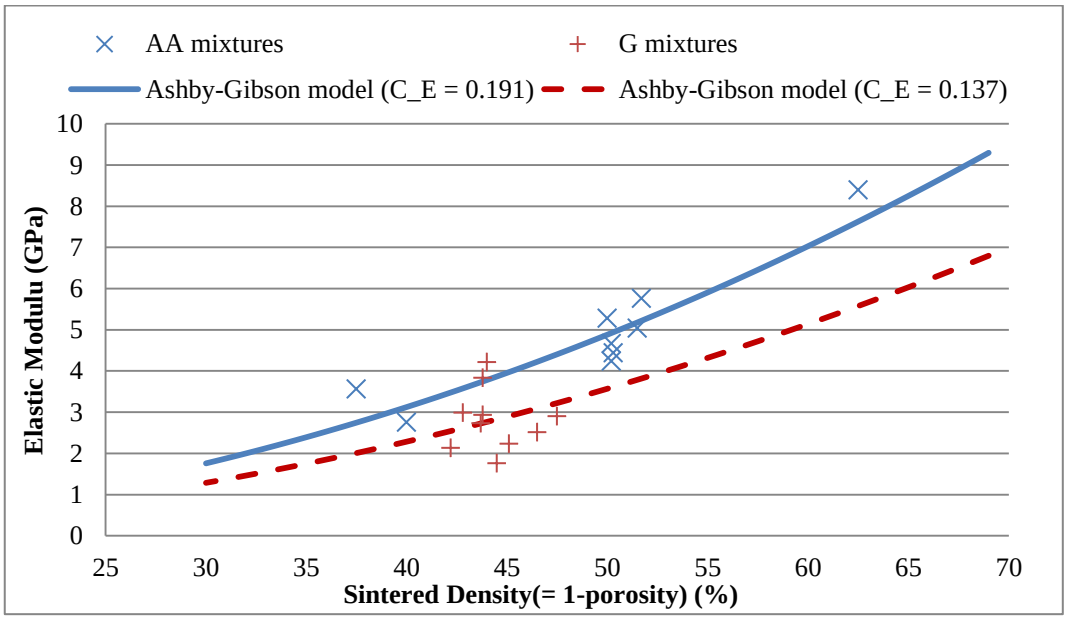

Figure 38: Elastic moduli vs density of sintered samples

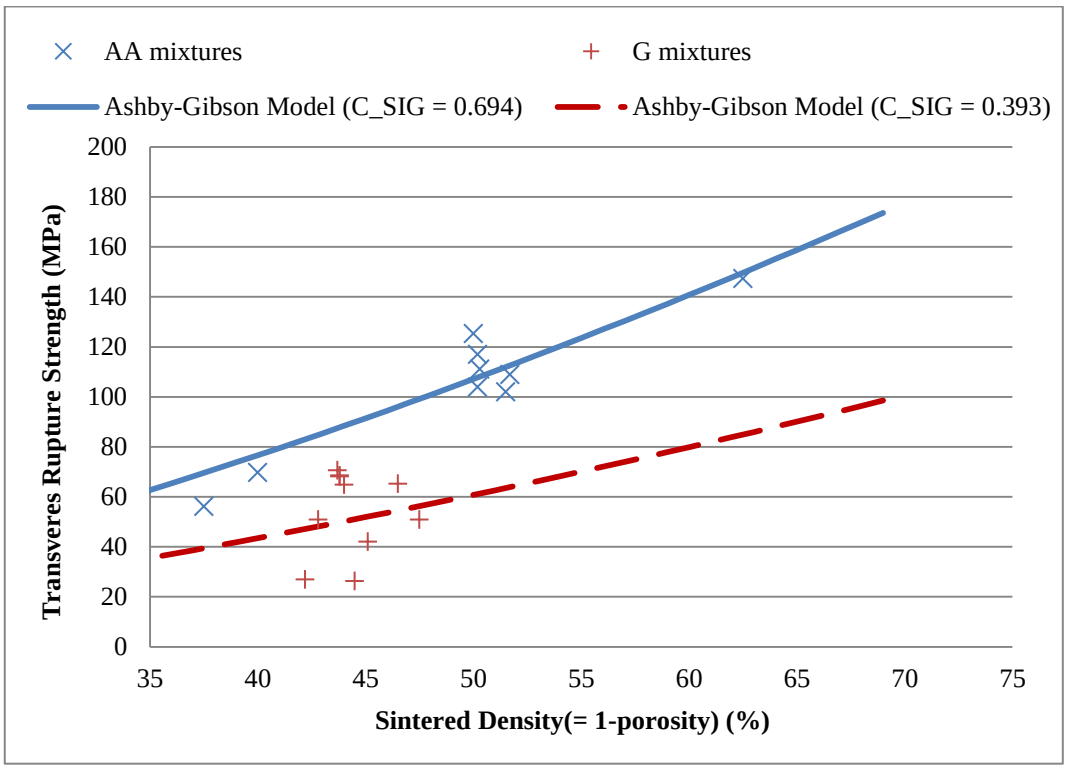

Figure 39: Transverse rupture strength vs porosity

For both the Young's modulus and transverse rupture strength, the Ashby-Gibson models predict the values reasonably well. As can be seen from the mean square error plots, Figure 36 and Figure 37, a clear minimum error is found for each parameter and powder. The average error of the prediction is below 10 % for the elastic moduli and below 8 % for the transverse rupture strength for the AA mixtures. However, for the G mixtures, the average errors were 22 % for elastic moduli and 32 % for the transverse rupture strength. It should be noted that the AA powder mixtures spanned a range of densities from 35 to 65 %, while the G powder mixtures were clustered over a narrower range, from 40 to 50 %.

To investigate the effect which the initial space holder particle size has on the porosity structure and hence the mechanical strength, the average strength and elastic modulus of samples with similar porosities but different initial space holder particle size ranges were compared. By doing this it essentially removes the effects of porosity on the samples and it makes it possible to isolate the effects of initial space holder particle size. The results of doing this are shown in Table 15.

Table 15: Average properties for different mixtures

Mixture designation	Macropore size (µm)	Relative density (%)	Elastic modulus (GPa)	Rupture strength (MPa)
AA 250-450	302.80	50.67	5.16	115.06
AA 425-560	385.22	50.63	4.65	107.56
G 250-450	507.75	43.83	3.43	60.57
G 425-560	498.67	43.17	2.29	34.66

As is shown in Table 15, the mechanical properties are affected not only by the level of porosity or density of the sample, but also by the initial space holder particle size range, which in turn influences the average macropore size. As the initial space holder particle sizes increase, the elastic moduli and rupture strength decreases.

When considering the difference in mechanical properties between the mixtures, it is found that the AA mixtures typically display a greater elastic modulus and rupture strength than that the G mixtures. As explained in section 7.1, the TiAA powder has a typical particle size which is half that of TiG powder. It is well-known that smaller particles have a higher sintering potential due to their increased surface area. As such, the smaller AA powder samples result in a denser metallic skeletal network, with smaller, more spherical pores after sintering. This results in a stronger, yet less stiff material. Note that strength and elastic modulus for typical sintered materials are directly related to the (micro)porosity (German, 1996).

When considering the mechanical properties of mixtures G 250–450 and G 425-560 from Table 15, they are found to differ, irrespective of the fact that their average macropore size and relative densities are the same. When studying

their micropore distribution, as in shown in Figure 35, it is found to be similar. However, their macropore size distribution differs, see Figure 34. For mixture G 425-560, 41.3 % of the pores are larger than 425 µm while only 29.4 % of pores are larger than 425 µm for G 250–450. These results indicate that a higher percentage of larger pores yields a foam with a lower structural integrity and thus weaker mechanical properties, which, as explained in section 4.6.3, contradicts work done by Tuncer *et al*. but follows similar findings to that of Amingo *et al.*

7.9. Correlating data

In order to review the results of this study in context, the current results were compared to similar studies documented in literature. The two main mechanical properties, rupture strength and elastic modulus, were evaluated along with titanium powder and space holder powder particle size and final foam density.

7.9.1. Production parameters

A selection of studies with similar production parameters to this were chosen from literature for comparison. Table 16, summarises the production parameters from each of these studies, along with the references for each. In Table 16 the following abbreviations are used; compaction pressure (CPres), sintering temperature (STemp), sintering time (STime), commercial pure titanium of grade 3 (CPTi 3) and commercial pure titanium of grade 3 (CPTi 3) (ASTM Standard F1580, 2001).

Table 16: Production parameter comparison

Sample code	Sources	Titanium powder	Space holder	Production parameters
S1	(Imwinkelried, 2007)	CPTi 3, < 45 µm, hydride–dehydride	$NH_4)HCO_3$, 425-710 µm	CPres : 100 MPa STemp = 1300 ºC STime = 3 hours
S2	(Amingo, et al., 2011)	CPTi 4, d50 = 25-40 µm, hydride–dehydride	$(NH_4)HCO_3$, 250-500 µm	CPres: 100 MPa STemp = 1300 ºC STime = 2 hours
S2	(Amingo, et al., 2011)	CPTi 4, d50 = 25-40 µm, hydride–dehydride	$(NH_4)HCO_3$, 500-100 µm	CPres: 100 MPa STemp = 1300 ºC STime = 2 hours
AA	Current research	CPTi 3, < 45 µm, hydride–dehydride	$(NH_4)HCO_3$, 0-710 µm	CPres: 100 MPa STemp = 1200 ºC STime = 2 hours
G	Current research	CPTi 3, < 75 µm, hydride–dehydride	$(NH_4)HCO_3$, 250-710 µm	CPres: 100 MPa STemp = 1200 ºC STime = 2 hours

All samples shown in Table 16 were produced using the same compaction pressure, space holder material and relatively similar titanium powder particle

sizes as this study. The sintering temperatures varied with 100 ºC and sintering times varied with 1 hour. In addition to all the similarities, the initial space holder particle sizes are also reported.

7.9.2. Mechanical strength comparison

Using the sample codes provided in Table 16, each sample is given a name similar to the naming scheme used through this document, i.e. the numbers following the sample identity refer to the space holder particle size range used for the particular mixture. The mechanical strengths reported for the mixtures evaluated in this study are similar to those reported in literature. The rupture strength follows the general Ashby-Gibson trend.

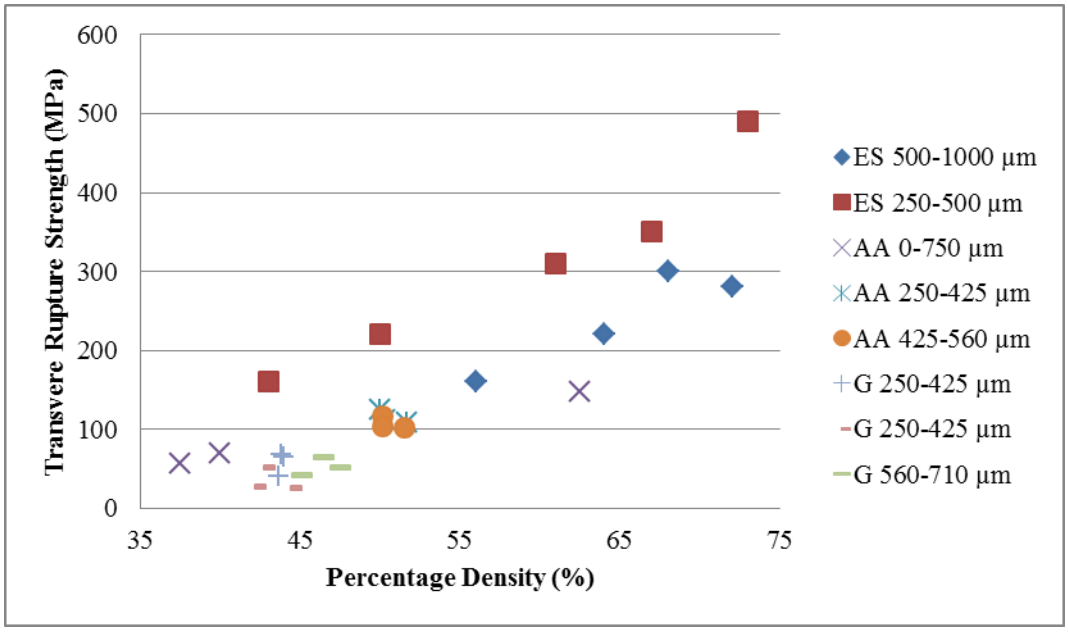

Figure 40: Comparison of transverse rupture strength results

From Figure 40, it is visible that although the general Ashby-Gibson relationship, equation (7), is followed, the strengths for the mixtures from this study are typically lower yield than those reported in similar studies from literature. As most of the published data is from samples that were typically sintered at higher temperatures and for longer durations, resulting in higher final density, this is not an anomalous result. When comparing samples of same sintering conditions and space holder particle size, the general trend of the strength decreasing as the space holder particle sizes increases holds true.

7.9.3. Elastic modulus comparison

Figure 43 shows the comparison of the reported elastic modulus from literature against the mixtures evaluated in this study. Unlike the similarities in the rapture

strengths, Figure 41 shows a relatively large difference between the elastic moduli of the samples from this study compared to those from literature.

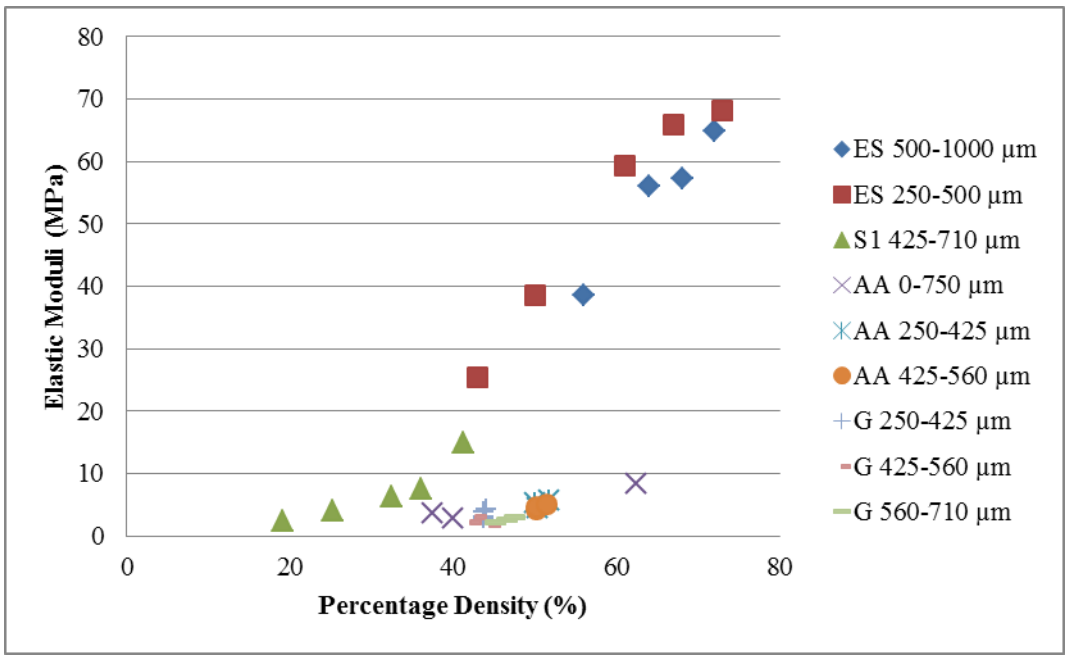

Figure 41: Comparison of elastic moduli results

Typically, the elastic moduli of the foams from this study are lower than those from literature. There are two possible reasons for this; it could be due to the contamination of the samples which resulted in making the samples more brittle, thus lowering the elastic modulus (section 7.2), or possibly the differences in the experimental procedures for measuring elastic modulus.

All the studies used three point bending tests to measure the mechanical properties. The elastic modulus is determined from the measured force and midpoint displacement, as described in equation (13) (section 4.5.2). To determine the sensitivity of the midpoint deflection measurement on the elastic modulus, the relationship between the midpoint displacement and strain is re-examined. From Hooke's Law ($\sigma = \varepsilon E$) and equation (13), the relationship between strain and the midpoint displacement is given by

$$\delta = \frac{\varepsilon L^2}{h} \tag{14}$$

Where:
δ = the deflection at midpoint (m).
ε = strain,
h = thickness of sample (m),
L = free length between supports (m),

As the elastic modulus is determined by averaging the value as calculated using equation (13) over a range of force-displacement, or equally stress-strain values in

the linear elastic region, the sensitivity of the displacement measurement as it relates to a specific strain value is examined. Using equation (14) and taking into account the different setups used to determine the elastic modulus in each study, the calculated difference in deflection required to obtain 1 % strain for each study is shown in Table 17. The results show that the deflection required to produce 1% strain in the samples from this study is half that of the S1 study, while twice that of the S2 study.

Table 17: Calculated midpoint deflection for 1 % strain for the powder mixtures G and AA, as compared to studies S1 and S2.

Sample code	Strain	Free length between supports (mm)	Sample thickness (mm)	midpoint deflection (mm)	Ram descending rate (mm/min)
G	1 %	25.4	5.6	0.19	1
AA	1 %	25.4	5.6	0.19	1
S1	1 %	30	4	0.38	1
S2	1 %	16	5.23	0.08	30

As mentioned in section 5.2.19, the resolution of the ram's displacement for this study is 0.04 mm, representing a potential 21 % error in the displacement measurement at 1 % strain. Assuming similar resolution for the measurements used for S1 and S2, and noting that the ram descending rate is much higher for S2, the differences between the reported elastic modulus of S2 and those from this study could be within the experimental error measurement of both studies.

7.10. Improving production processes

In hindsight there are a couple of things which could be done differently to improve the production process of the samples. The follow are ways of improving the process:

- Debind the samples in a vacuum or inert atmostphere (in argon), this will reduce the amount of contamination which occurs during the process.
- Remove the requirement for PEG from the mixture. The PEG was added to the mixture to act as a binding and lubricant. As the compaction pressure is relatively low, there is no need for PEG. Removing PEG from the mixture will result in reducing the required debinding temperature, which will reduce the amount of contamination which occurs during the process, as PEG debinds at temperatures close to the critical oxidation temperature of titanium.
- Compact larger specimens and machine the dimension of the specimen to the exact requirements.
- Investigate the feasibility of conducting the debinding of the ammonium bicarbonate in the vacuum furnace

7.11. Areas for further studies

During this study certain problems and interesting phenomena were discovered, however due to time constraints an in depth study each case was not possible or fell out of the scope of this project. The follow are key areas which could require some future research:

- Determine and take into account the compliance of the three-point-bending test ridge. This is required to adjust the measured displacement and with the expected deformation of the test ridge under loading.
- A comparison of a 3D tomography and 2D quantitative image analysis, how they relate to each other and accuracy.
- Conduct porosimetry on the specimens to get a better understanding of the interconnectivity of the open pores.
- A comparison of wall thickness to space holder particle size, certain work is contradicting.
- Investigate the effects on increasing the sintering temperature or duration on the macropore and micropore size distributions.

8. CONCLUSION

Open-pore titanium foams were created using the space holder production process. By altering the titanium powder and the space holder particle size distributions, the porosity of the final foam were controlled and, coherently, also the mechanical properties. The recorded mechanical properties were altered sufficiently to reduce the typical mechanical strength and elastic moduli to match that which is expected for bone.

The measured powder characteristics, particle size distribution and chemical composition, match that of the characteristics supplied by the suppliers of both titanium powders. It was found that different powder characteristics have a large influence on the mechanical properties. The smaller particle size powder, TiAA, was found to sinter more densely than its larger particle size counterpart, TiG.

The use of PEG as a lubricant was found to have a negative effect on the final sintered samples. This is due to the decomposition temperature of PEG being too close to the critical onset temperature of oxidation for both titanium powders. It is concluded that due to the low compaction pressure of the samples, the need for a lubricant is unnecessary and should be removed for further studies.

The open, interconnected pores network created during the manufacturing process were found to be favourable for osseointegration.

From the pore size distribution, it was found that the pores distribution resulted in pores with a bimodal distribution. The first mode was creating by isolated, individual macropores which did not interconnect with other macropores and as a result was slightly smaller than the initial space holder particle size, due to sintering. The second mode was created by the interconnectivity of two or more macropores, which results in pores typically much larger than the initial space holder particle size range.

The mechanical properties of the produced samples were found to match the typical curve of the Ashby-Gibson relationship for both elastic moduli and strength. It was however found, that the elastic modulus and strength of the samples were lower than that recorded by other researchers. This is found to be a combination of contaminates found in the samples, resulting in more brittle samples, and possibly experimental error, due to experimental setup differences.

9. REFERENCES

Amingo, V. et al., 2011. Analysis of bending strength of porous titanium processed by space holder method. *Powder Metallurgy*, 54(1), pp. 67-70.

Arifvianto, B. & Zouh, J., 2014. Fabrication of Metallic Biomedical Scaffolds with the Space Holder Method: A Review. *Materials*, 7(5), pp. 3588-3622.

Ashby, M. F. et al., 2000. Design formulae for simple structures. In: *Metal foams: A design guide.* first ed. Warrendale: Butterworth-Heinemann, pp. 66-68.

ASTM Standard 925, 2003. *"Production and Preparation of Powder Metallurgy (P/M) Test Specimens", ASTM International, West Conshohocken, PA, 2003.* DOI: 10.1520/B0925-03, www.astm.org.

ASTM Standard B417, 2000. *"Standard Test Method for Apparent Density of Non-Free-Flowing Metal Powders Using the Carney Funnel", ASTM International, West Conshohocken, PA, 2000.* DOI: 10.1520/B0417-00, www.astm.org.

ASTM Standard B528, 2005. *"Standard Test Method for Transverse Rupture Strength of Metal Powder Specimens", ASTM International, West Conshohocken, PA, 2005.* DOI: 10.1520/B0528-05, www.astm.org.

ASTM Standard C136, 2006. *"Standard Test Method for Sieve Analysis of Fine and Coarse Aggregates", ASTM International, West Conshohocken, PA, 2006.* DOI: 10.1520/C0136-06, www.astm.org.

ASTM Standard F1580, 2001. *"Standard Specification for Titanium and Titanium-6 Aluminum-4 Vanadium Alloy Powders for Coatings of Surgical Implants", ASTM International, West Conshohocken, PA, 2001.* DOI: 10.1520/F1580-01.

ASTM Standards B328, 2003. *"Standard Test Method for Density, Oil Content, and Interconnected Porosity of Sintered Metal Structural Parts and Oil-Impregnated Bearings", ASTM International, West Conshohocken, PA, 2003.* DOI: 10.1520/B0328-96R03.

B.K, A., 1991. *X-ray Spectroscopy.* 2nd ed. Berlin: Springer-verlag.

Black, J. & Hastings, G., 1998. *Handbook of Biomaterial Properties.* 1st ed. London: Chapman and Hall.

Bram, M. et al., 2006. Implant surgery: How bone bonds to PM titanium. *Metal Powder Report*, 61(2), pp. 26-31.

Chino, Y. & Dunand, D., 2009. Creating aligned, elongated pores in titanium foams by swaging of preforms with ductile space-holder. *Advance Engineering Materials*, 11(2), pp. 52-55.

Duncand, D. C., 2004. Processinf of titanium foams. *Advance Engineering Materials*, 6(6), pp. 369-376.

Ellis, R., 2008. *The optimisation of a highly effective, homogenising metal powder mixer,* Stellenbosch: Department of Mechanical and Mechatronical Engineering, Stellenbosch University.

German, R., 1985. *Liquid phase sintering.* New York: Plenum Press.

German, R., 1996. *Sintering theory and Practice.* New York: John Wiley and Sons, Inc..

Gibson, L. J. & Ashby, M. F., 1988. *Cellular Solids; Structure and Properties.* 2 ed. s.l.:Cambridge University Press.

Gibson, L. J. & Ashby, M. F., 1997. Cellular solids: Structure and properties. *Cambridge: Cambridge Univeristy Press,* Issue 2.

Hattiangadi, A. & Bandyopadhyay, A., 2000. Strength degradation of nonrandom porous ceramic structures under uniaxial compressive loading. *Journal of the American Ceramic Society,* 83(11), pp. 2730-2736.

Imwinkelried, T., 2007. Mechanical properties of open-pore titanium foam. *Journal of biomedical materials research Part A,* 81(4), pp. 964-970.

Klokkevold, P. & Jovanovic, S., 2002. Advance implant and bone grafting techniques. In: *Carranza's Clinical Periodontology.* 12 ed. Missouri: Elsevier, pp. 907-908.

Marais, J., 2007. *The design, manufacture and testing of a highly effective, homogenising metal powder mixer,* Stellenbosch: Department of Mechanical and Mechatronical Engineering, Stellenbosch University.

Nouri, A., 2008. *Novel metal structures through powder metallurgy for biomedical applications.,* Melbourne: Institute for Technology Research and Innovation, Deakin University.

Nouri, A., Hodgson, P. D. & Wen, C., 2010. Biomimetic Porous Titanium Scaffolds for Orthopedic and Dental Applications. In: A. Mukherjee, ed. *Biomimetics, Learning from Nature.* Rijeka: InTech, pp. 416-450.

Pan, J. et al., 2009. Densification of Powder Compact Containing Large and Small Pores. *Journal of the American Ceramic Society,* 92(7), pp. 1415-1418.

Ryan, G., Pandit, A. & Apatsidis, D. P., 2006. Fabrication methods of porous metal for use in orthopaedic applications. *Biomaterials,* 27(13), pp. 2561-2670.

Shafirovich, E., Teoh, S. K. & Varma, A., 2008. Combustion of levitated titanium particles in air. *Combustion and flame,* 152(2), pp. 262-271.

Spoerke, E. D. et al., 2008. Titanium with aligned, elongated pores for orthopedic tissue engineering applications. *Journal of Biomedical Materials Research,* 84(2), pp. 402-412.

Taylor, B. & Weidmann, E., 2008. *Struers A/S.* [Online] Available at: http://www.struers.co.uk/resources/elements/12/104827/Application_Note_Titani

um_English.pdf
[Accessed 28 07 2014].

Thomson, R. C., Wake, M. C., Yaszemski, M. J. & Mikos, A. G., 1995. Biodegradable polymer scaffolds to regenerate organs. *Advances in Polymer Science*, 122(1), pp. 245-274.

Tuncer, N., Arslan, G., Maire, E. & Salvo, L., 2011. Investigation of spacer size effect on architecture and mechanical properties of porous titanium. *Material Science Engineering*, Volume 530, pp. 633-642.

van Zyl, W. H., 2010. *Investigation on the production of porous titanium for bio medical applications*, Stellenbosch: Department of Mechanical and Mechatronical Engineering, Stellenbosch University.

Wen, C. et al., 2001. Processing of biocompatible porous Ti and Mg. *Scripta Materialia*, 45(10), pp. 1147-1153.

Wenjuan, N., Chenguang, B., Guibao, Q. & Qiang, W., 2008. Processing and properties of porous titanium using space holder techniques. *Material Science and Engineering A*, 506(2), pp. 148-151.

Wisutmethangoon, S., Prathumrat, N., Lek, S. & Thawatchai, P., 2008. Synthesis and characterization of Porous titanium. *Songklanakarin Journal of Science and Technology*, 30(4), pp. 509-513.

APPENDIX A. VOID FRACTION CALCULATION

In this appendix, the procedure is explained for calculating the required amount of each powder constituencies required within a mixture. Before it is possible to calculate estimated amount, an experiment with estimated ideal parameters was conducted in order to obtain relative estimation of the global void fraction and shrinkage.

Initial experiment

For the initial experiment, the mass of CPTi, PEG and ABC were each estimated to give a final material of approximately 60 % dense, 40 % porosity. The compaction pressure and the sintering duration were kept constant at 100 MPa and 1200 ºC, respectively. The follow steps were taken within the initial experiment to determine the shrinkage percentage and the void fraction:

- The volume of the green compact, V_g, was calculated:

$$V_g = length \times width \times thickness \quad (15)$$

Where:

V_g = the volume of the green sample in cm^3,

length = the length of the green sample in cm,

width = the width of the green sample in cm,

thickness = the length of the green sample cm.

- The void (total porosity) volume is determined as:

$$V_{void} = \left(V_g - V_{gPEG} - V_{gTi} - V_{gABC}\right) \quad (16)$$

Where:

V_{gABC} = the volume which ABC occupies of the green sample in cm^3,

V_{gPEG} = the volume which PEG occupies of the green sample in cm^3,

V_{gTi} = the volume which titanium occupies of the green sample in cm^3,

V_{void} = the void volume which occupies the green sample in cm^3.

The volume of each powder was calculated by taking the mass of each constituent and multiplying it by the solid density of the constituents

- The green density, ρ_g, is calculated as:

$$\rho_g = \frac{m_g}{V_g} \quad (17)$$

Where:

ρ_g = the green density of the sample in $\frac{g}{cm^3}$,

m_g = the mass of the green sample in g,

- The void percentage is calculated:

$$\%\ void = \frac{V_{void}}{V_g} \times 100\ \% \quad (18)$$

- Post sintering, the percentage of sintering shrinkage in each dimension is calculated by comparing the green and sintered dimensions (length, width and thickness):

$$\%\ shrinkage = \frac{sintered\ dimension - green\ dimension}{green\ dimension} \times 100\ \% \quad (19)$$

An average of all the dimensions is taken as the percentage of sintering shrinkage.

Establish procedure

- The volume of the green compact, V_g, for the new set of experiments is calculated using equation (15):
- The estimated volume of the sintered sample is calculated assuming the percentage of sintering shrinkage is isotropic:

$$V_s \cong V_g * (1 - \%\ shrinkage)^3 \quad (20)$$

Where:

V_s = the volume of the sintered sample in cm^3.

- The mass of titanium powder required is calculated by multiplying the volume of the sintered sample with that of the desired sintered density (1.376 g/cm^3, refer to section 5.2.3) of the sintered sample:

$$m_{sTi} = V_s \times \rho_{desired} \quad (21)$$

Where:

m_{sTi} = the mass of titanium powder in g,

$\rho_{desired}$ = the desired density of the sintered specimen in g/cm^3.

- The actual volume per sample which the titanium powder occupies is calculated by multiplying the mass of titanium powder needed per sample by the actually density of pure titanium, ρ_{Ti}.

$$V_{gTi} = m_{sTi} \times \rho_{Ti} \quad (22)$$

Where:

V_{gTi} = the volume which titanium occupies of the green sample in cm^3,

ρ_{Ti} = the density of pure titanium powder g/cm^3.

- The volume percentage of PEG added is predefined (typically in the region of 2 *vol%*) and accordingly the volume which the PEG occupies is calculated:

$$V_{gPEG} = (Percentage\ vol\%\ of\ PEG)V_g \quad (23)$$

Where:

V_{gPEG} = the volume which PEG occupies of the green sample in cm^3,

- Similarly to equation (18), the void volume, $V_{void,}$ can be calculated by using the established void percentage in the initial experiments. Here the void volume is estimated by assuming it is the same value as in the initial experiment.

- The mass of PEG is calculated by multiplying the volume of the PEG in the sample with the density of PEG:

$$m_{gPEG} = V_{gPEG} \times \rho_{PEG} \quad (24)$$

Where:

m_{gPEG} = the mass of PEG powder required in the green state in g,

ρ_{PEG} = the density of pure PEG powder g/cm^3.

- The volume which ammonium bicarbonate will occupy is calculated as the remaining volume of the sample:

$$V_{gABC} = \left(V_g - V_{gPEG} - V_{gTi} - V_{void}\right) \quad (25)$$

Where:

V_{gABC} = the volume which Ammonium bicarbonate occupies of the green sample in cm^3,

V_{void} = the void volume which occupies the green sample in cm^3.

- Finally, the mass of ammonium bicarbonate can be calculated by multiplying the volume of ammonium bicarbonate with the density of ammonium bicarbonate.

$$m_{gABC} = V_{gABC} \times \rho_{ABC} \quad (26)$$

Where:

m_{gABC} = the mass of Ammonium Bicarbonate powder required in the green state in g,

ρ_{PEG} = the density of pure Ammonium Bicarbonate powder g/cm^3.

APPENDIX B. FLEXURE STRENGTH

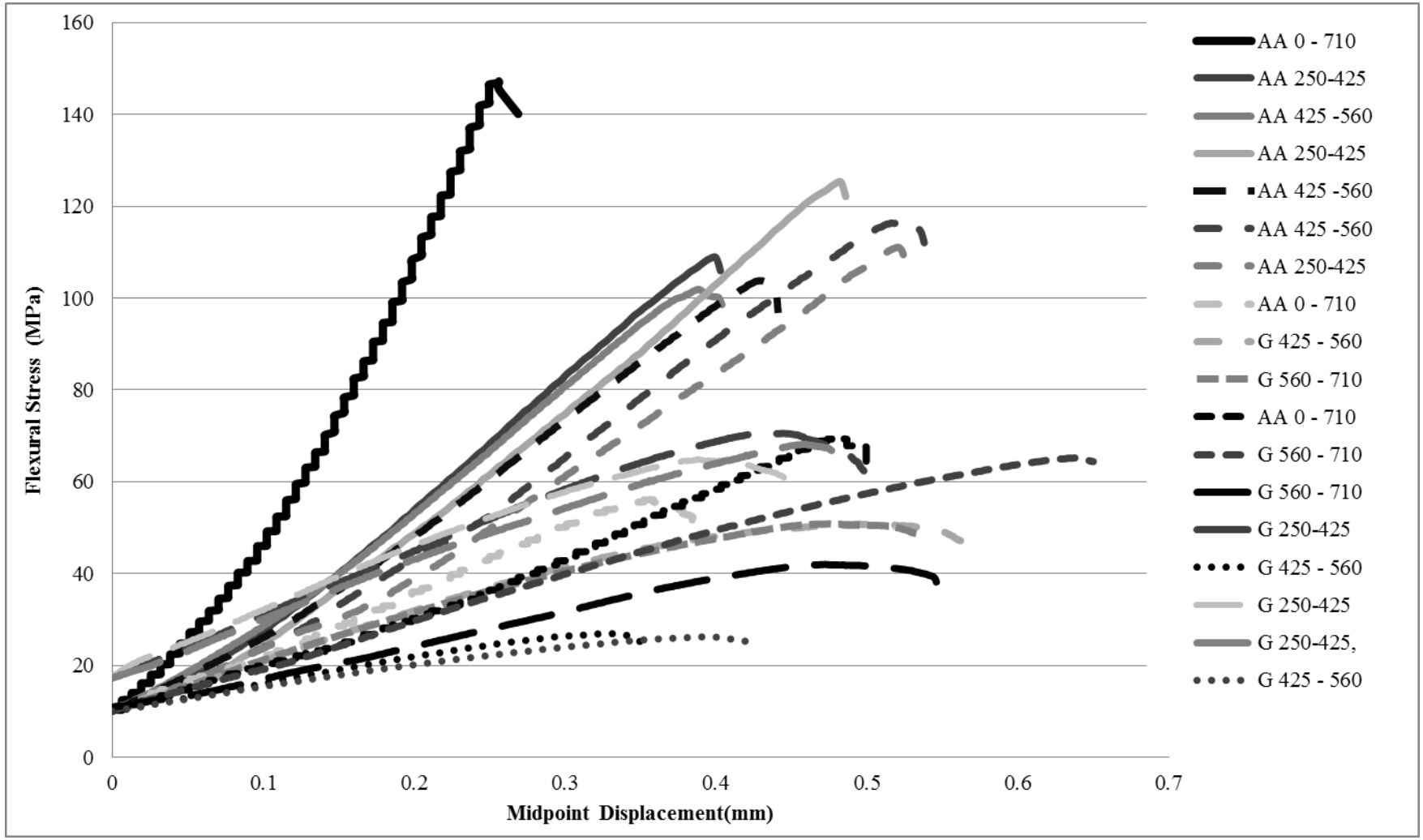

Figure 42: Flexure Stress vs Displacement

APPENDIX C. PORE SIZE DISTRIBUTION ANALYSIS

The pore size distribution was determined by using light micrographs of sample which were mounted in epoxy resin. A luminescent powder was mixed into the epoxy so that when the epoxy is exposed to a light source, the luminescent powder will absorb the light. This attribute is used to make the pores display black on micrographs taken using a reflective microscopes, which makes it easier to isolate the different pore structures.

The unedited micrographs, refer to Figure 43 for example, are important into ImageJ, image analysis software, where the colour threshold are changed to either select the large pores, refer to Figure 44, or to select the small pores, refer to Figure 45.

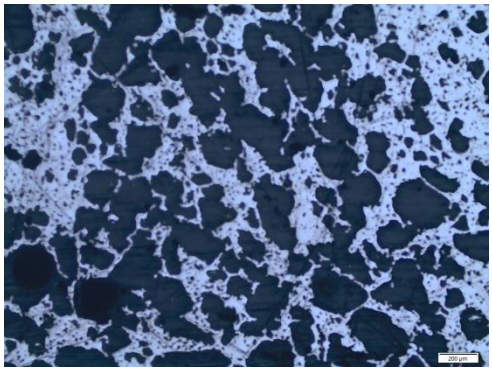

Figure 43: Unedited micrograph

Typically the colour difference between the large pores and small pores are significant enough so that you need to measure them independently. If both large and small pores are measured simultaneously, error is introduced into the measurement. This error is cause by the pixel surround the macropores becoming also highlighted and increasing the macro pore size. Besides the increase in individual pores size it is typically found that the interconnectivity falsely increases as the small section of base metal between pores also become selected.

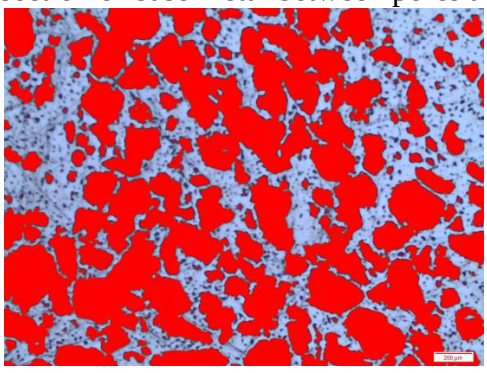

Figure 44: Colour threshold changed to select pores larger than 3000 µm^2

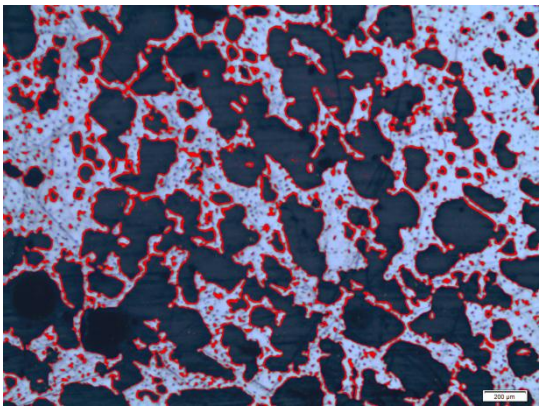

Figure 45: Colour threshold changed to select pores smaller than 3000 µm^2

After both large and small pores are selected it is required to set the scale of the image. This is done by drawing a line over the scale bar and entering the known length. Once this is completed a particle analysis done on both samples. For the large pores, only pores with a greater area than 3000 µm^2 are selected and for the small pores, only pore with a smaller area than 3000 µm^2.

The results of the particle analysis are imported into a spreadsheet where after the hydraulic diameter is determined of each pore basics on the area measure from the particle size analysis.